TU
TECHNISCHE
UNIVERSITÄT
WIEN

DIPLOMARBEIT

Fabrication and Evaluation of Test Structures for Precise Dose Control of Ion Implantation Equipment in Semiconductor Manufacturing

zur Erlangung des akademischen Grades

Diplom-Ingenieur/in

im Rahmen des Studiums

Masterstudium Technische Physik

eingereicht von

Andrea Fugger
Matrikelnummer 01621480

ausgeführt am Institut für Angewandte Physik
der Fakultät für Physik der Technischen Universität Wien
(in Zusammenarbeit mit Infineon Technologies Austria AG)

Betreuung
Betreuer/in: Univ.Prof. Dipl.-Ing. Dr.techn. Markus Valtiner
Mitwirkung: Dr.techn. Ingo Muri (Infineon Technologies)

Wien, 31.03.2023

_____(Unterschrift Verfasser/in)_____   _____(Unterschrift Betreuer/in)_____

Abstract

As process windows for microchip fabrication become smaller, more accurate process controls are necessary, especially for ion implantation. This work focusses on developing test methods and structures for fast and precise dose monitoring for p- and n-type implants into silicon with productive doses and evaluating them against an existing process on unstructured wafers. The structures are based on layouts provided by Infineon Technologies Austria AG and were tested with implant doses in the range of $10^{13}\,\mathrm{cm}^{-2}$ to $10^{15}\,\mathrm{cm}^{-2}$ regarding sensitivity, uniformity and accuracy. First results show an improved uniformity and stability through the use of statistical methods on unstructured wafers. The test structures were measured with a 4-point probe measurement and allow the monitoring of p- and n-type implants with a defined geometry.

Eidesstattliche Erklärung

Ich erkläre an Eides statt, dass die vorliegende Arbeit nach den anerkannten Grundsätzen für wissenschaftliche Abhandlungen von mir selbstständig erstellt wurde. Alle verwendeten Hilfsmittel, insbesondere die zugrunde gelegte Literatur, sind in dieser Arbeit genannt und aufgelistet. Die aus den Quellen wörtlich entnommenen Stellen, sind als solche kenntlich gemacht.

Das Thema dieser Arbeit wurde von mir bisher weder im In- noch Ausland einer Beurteilerin/einem Beurteiler zur Begutachtung in irgendeiner Form als Prüfungsarbeit vorgelegt. Diese Arbeit stimmt mit der von den Begutachterinnen/Begutachtern beurteilten Arbeit überein.

Ich nehme zur Kenntnis, dass die vorgelegte Arbeit mit geeigneten und dem derzeitigen Stand der Technik entsprechenden Mitteln (Plagiat-Erkennungssoftware) elektronisch-technisch überprüft wird. Dies stellt einerseits sicher, dass bei der Erstellung der hier vorgelegten Arbeit die hohen Qualitätsvorgaben im Rahmen der geltenden Regeln zur Sicherung guter wissenschaftlicher Praxis "Code of Conduct" an der TU Wien eingehalten wurden. Zum anderen werden durch einen Abgleich mit anderen studentischen Abschlussarbeiten Verletzungen meines persönlichen Urheberrechts vermieden.

Acknowledgements

Contents

Chapter 1

Introduction

The trend in semiconductor technologies goes to ever smaller and more efficient devices. To accomplish this, new technology generations allow fewer variations in the production process, resulting in a need to achieve a higher precision in tool monitoring. One of the critical processes during semiconductor microchip fabrication is the implantation of dopants.

The determination of the differences in electrical parameters based on dopant concentrations in silicon has been a matter of interest for at least 80 years. At first the properties of silicon doped in the melt were determined.[1], [2] With the revolutionary addition of an annealing step after the bombardment of a material with ions by Shockley [3], ion implantation started its way to become one of the essential process steps in semiconductor fabrication. With this also came the need to accurately measure the implanted ion concentration. Thermal wave techniques proved to be an effective way of measuring the ion implantation dose for productive wafers, since the measurement is non-destructive and the results show a high correlation to the electrical parameters influenced by the implant. [4] While thermal wave measurement techniques are without a doubt useful for measuring the implanted dose immediately, as it uses the damage generated by the implantation, without the need for an annealing step, they do not account for the final electrically active dose in the material. They are best used for doses where the amorphisation of the target material is not an issue. [5]

Another popular way to monitor ion implantations is through the use of the sheet resistance. A direct comparison between those two measurements from Falk et al. [6] showed, that both systems react with different sensitivities to the implanted dose, due to the non-linear relationship between the dose and the measured parameter and their different reaction to other process parameters. The measured sheet resistance for example is more or less constant for differing beam currents, but can be affected by the annealing step or the removal of a scattering oxide. A thermal wave measurement on the other hand is based on the damage caused by ion implantation and also measures the oxide thickness, no annealing step or oxide removal is needed. It is not influenced by the bulk doping of the wafer. The impact of a change in beam current is higher for thermal wave measurements, than for sheet resistance. This might lead to misinterpretations of the results, if the beam current varies. [6] While both sheet resistance measurement and thermal wave measurement offer advantages, they both use a whole wafer as a sample. As such the geometry

of the measured region is only defined by the crystal damage or by the change in dopant type. Using test structures with defined geometry would eliminate the need for corrective factors and for surface-near implants. This would allow the determination of ion implanter variations under different conditions, that are closer to productive conditions.

This thesis aims to fabricate and evaluate such semiconductor test structures to provide an accurate way of monitoring p- and n-type implants into silicon in a wide range of implant doses and energies with sufficient accuracy. Additionally the effect of multiple implants compared to single implant processes is assessed.

Chapter 2

Fundamentals

This chapter aims to provide an overview of the most important concepts that will be used during this thesis.

2.1 Silicon Fundamentals

Silicon is a semiconductor that crystallises in the diamond structure with covalent bonds and shows the typical bandstructure for semiconductors with a valence and a conduction band made up of subbands, separated by a bandgap without allowed energy states, as seen in fig. 2.1. The difference between the highest possible state in the valence band and the lowest state in the conduction band is the bandgap E_g. For silicon this difference is $1.12\,\text{eV}$ at room temperature. The minimum of the conduction band and the maximum of the valence band are offset against each other, leading to an indirect band gap for Silicon.

Through the use of dopant atoms, the bandgap can be reduced, by creating allowed states within the gap. Dopant atoms are classified into donors and acceptors. Donors are substitutional atoms with one more valence electron than silicon and donate this electron to the conduction band. A material doped with donors is called n-type. Acceptors also take the place of a silicon atom in the lattice, but they have one valence electron less and accept an electron, while leaving a positively charged hole in the valence band. A material doped with acceptors is called p-type. For silicon with 4 valence electrons, boron acts as an acceptor and phosphorous as a donor. The energy states of donors and acceptors are close to the allowed bands. For boron it is located $0.044\,\text{eV}$ above the valence band edge, while the phosphorous state is $0.046\,\text{eV}$ below the edge of the conduction band. Their small ionization energies result in ionized dopant atoms at room temperature, meaning, that dopant atoms at lattice sites are electrically active. [7, pp.1-23]

2.2 Implanter

During an ion implantation process a beam of accelerated ions is scanned over a wafer. The ions stop within the wafer through elastic nuclear collisions and electronic deceleration. In a first approximation, the implanted profile can be described by a gaussian
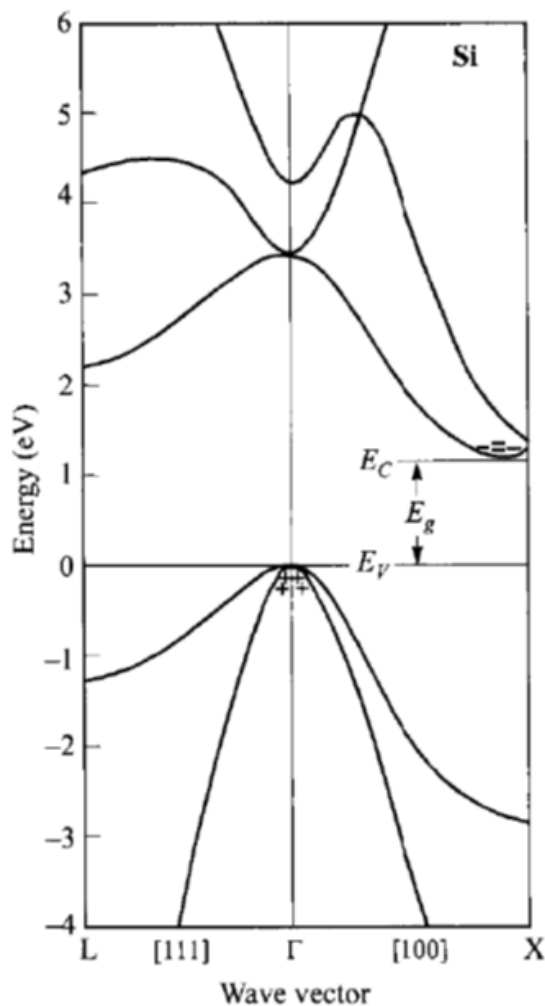
Figure 2.1: Energy band structure of Silicon. Used with permission of
Wiley-Interscience from [7, p. 14]; permission conveyed through
Copyright Clearance Center, Inc.

distribution. The depth of the profile peak is determined by the initial energy and its width is determined by statistical straggling. In general, for higher implantation energies the straggling increases leading to a wider distribution of the profile and a reduced peak height. If the direction of the incident ion beam aligns with a particular axis of the silicon crystal, channeling occurs. Under channeling conditions the chance of nuclear collisions of an incident ion is reduced dramatically enabling the ion to reach deeper into the crystal. Channeling can be avoided by tilting and twisting the wafer, using a scattering oxide or by a pre amorphisation implant. The collisions of the incident ions with the silicon atoms generate crystal damage in the form of vacancies and interstitial Si in the target material. The depth profile of the generated defects is similar to the energy deposition along the scattering path of the implanted ions. The implant damage depends on the implant energy, the ion mass and the final dose. For high values of those parameters the crystal can be amorphized. After the implantation the dopant must be thermally activated and incorporated into the crystal structure at a substitutional site. This can be done by a fast annealing step at high temperatures, like Rapid Thermal Annealing

(RTA). Typically this process uses temperatures above 1000°C for short durations in the range of 10 s to 60 s. Through the short annealing time the dopant ions do not diffuse far. Their depth distribution can still be approximated by the distribution before the annealing step. [8] During the course of this thesis medium current ion implanters of the VIISta 900XP and VIISta 900 3D lines from Applied Materials were used. Figure 2.2 shows the beam transport system of such an implanter. In an ion source the process gas with the desired dopant species is ionized. Those ions are then extracted from the source and filtered. Depending on the chosen energy the ions are accelerated or decelerated in the accel/decel column, before a mass analysis takes place. The VIISta 900 3D plattform offers the possibility to adjust the beam shape by a quadrupole. In the scanner the beam is horizontally scanned with a frequency of about 1 kHz to broaden the effective beam to the width of the wafer. After the scanning the beam must be parallelized by a collimator to achieve the required angle accuracy of 0.1°. At the end, in the process chamber the wafer is moved by a mechanical system vertically through the scanned beam. The speed and amount of times the wafer passes through the beam depends on the achieved beam current and the required dose. [9] [10]
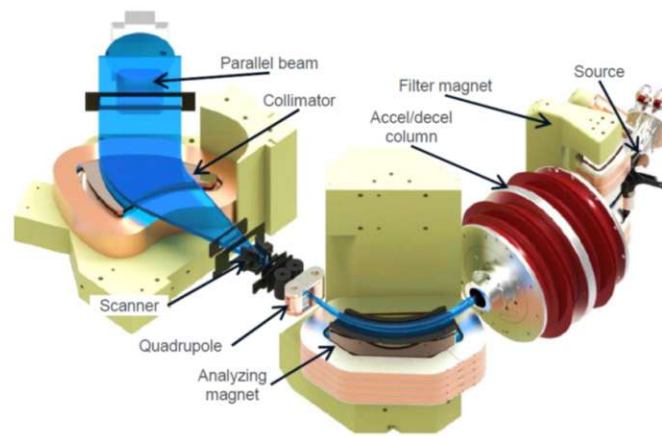
Figure 2.2: VIISta 900 3D beam transport system. Taken from [10]
©2014, IEEE

2.3 pn-Junction

In the event of neighbouring n-doped and p-doped areas within a semiconductor, an abrupt pn-junction is formed. If the impurity concentration on one side of the junction is significantly higher than on the other side, the junction is referred to as a one-sided abrupt pn-junction.

In thermal equilibrium "the condition of zero net electron and hole currents requires that the Fermi level must be constant throughout the sample."[7, p.81] In case of a one-sided pn-junction the depletion region extends farther into the lightly doped side than into the heavily doped side. As seen in fig. 2.3, a depletion region is created at the junction. The mobile charge carriers of this region recombine, leaving only the atomic cores of the dopants. An electric field is generated by the acceptor and donor ions. Integrating over the field results in the built-in potential Ψ_{bi}. At equilibrium the carrier densities on either side of the junction can be described by equation 2.1

10

$$\Psi_{bi} = \frac{kT}{q} ln \left(\frac{p_{p0}}{p_{n0}} \right) = \frac{kT}{q} ln \left(\frac{n_{n0}}{n_{p0}} \right) \qquad (2.1)$$

where n_{n0} and p_{n0} refer to the equilibrium concentrations of electrons and holes within the n-type side of the junction, while n_{p0} and p_{p0} describe the concentrations on the p-type side. The built-in potential can be used to calculate the width of the depletion region with formula 2.2.

$$W_D = \sqrt{\frac{2\epsilon_s \Psi_{bi}}{qN}} \qquad (2.2)$$

Here N is either the acceptor or donator impurity concentration, depending on which concentration is higher. The permittivity of the semiconductor is given by ϵ_s. For a junction under bias, Ψ_{bi} is replaced by $\Psi_{bi} - V$, where V is the applied voltage. The width of the depletion region is reduced or increased for forward or reverse bias. [7, pp. 80]

2.4 Metal-Semiconductor-junction

The information for this section was taken from [7, pp. 135-191].
At a Metal-semiconductor-junction the semiconductor Fermi level is changed to match that of the metal through bending the conduction and valence bands. A negative charge is build up on the metal side of the interface and a depletion layer is formed in the semiconductor. This results in a potential barrier $q\Phi_{Bn0}$, that limits the electron movement. For an n-type semiconductor the barrier can be described as $q\Phi_{Bn0} = \Phi_m - \chi$, where Φ_m is the work function of the metal and χ is the electron affinity of the semiconductor. For a p-doped semiconductor in contact with a metal, the barrier height is equal to the band gap minus this difference.
Concerning the band-diagram the metal-semiconductor junction is similar to an abrupt pn-junction. With this the width of the depletion layer is

$$W_D = \sqrt{\frac{2\epsilon_S}{qN_D} \left(\Psi_{bi} - V - \frac{kT}{q} \right)}, \qquad (2.3)$$

which is similar to eq. (2.2) under bias. The additional term kT/q is due to the tail of the majority-carrier distribution.
Sze [7] mentions 2 assumptions for the barrier height. Firstly both materials are in contact with each other, separated only by an interfacial layer. This layer has atomic dimensions, so it is transparent for electrons. Secondly only the semiconductor influences the interface states. This leads to 2 limiting cases, one were the surface states pin the Fermi level above the valence band and one were the surface states are neglected and the barrier is described by an ideal Schottky barrier.
For a metal-n-type Si this results in $q\Phi_{Bn0} = 0.27q\Phi_m - 0.52$. For contact with Si the formation of silicides is advantageous, as it allows for a higher reproducibility of the Schottky barriers. It is possible to adjust the height of the barrier either by choosing

p-region — | — n-region

Depletion region

Depletion charge $(N_D - N_A)$

Donor density (N_D)

$- W_{Dp}$

x

0 W_{Dn}

Acceptor density (N_A)

(a)

$\mathscr{E}$ 0 W_{Dn}

$- W_{Dp}$ x

Area = built-in potential ψ_{bi}

$- \mathscr{E}_m$

(b)

ψ_i

$- \psi_n$ ψ_{bi}

ψ_p

0 x

(c)

E_C

$q\psi_{bi}$

E_i

E_F $q\phi_p$ $q\psi_{Bp}$ $q\psi_p$ $q\phi_n$

E_V $- q\psi_n$ $q\psi_{Bn}$

(d)
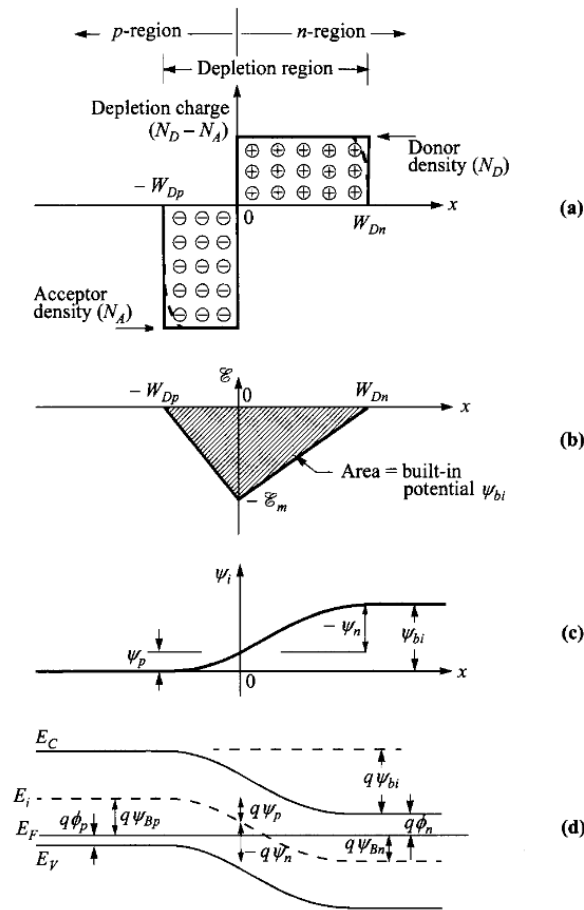
Figure 2.3: "Abrupt p-n junction in thermal equilibrium. (a)
Space-charge distribution. Dashed lines indicate corrections to
depletion approximation. (b) Electric-field distribution.(c)
Potential distribution where Ψ_{bi} the built-in potential. (d)
Energy-band diagram."[7, p. 80] Used with permission of
Wiley-Interscience from [7, p. 80]; permission conveyed through
Copyright Clearance Center, Inc.

a metal with a suitable work function or by changing the dopant concentration in the
semiconductor. A thin, highly doped layer on the semiconductor side of the junction
interface can be used to lower the barrier if its dopant type is the same as the dopant
type of the semiconductor. The current transport through the junction is dependent on
the majority carriers. During the main transport process at room temperature electrons
overcome the potential barrier starting from the semiconductor side. Alternative transport
processes are quantum tunneling, recombination, diffusion of electrons into the depletion
region and the injection of holes from the metal into the semiconductor. For high dopant
concentrations on the semiconductor side tunneling becomes the main process. It is a
characteristic of an ohmic metal-semiconductor junction. The Schottky barrier height for
n-type Si in contact with Ti or TiSi2 is below 0.6 V. In general the barrier is reduced
through the formation of the silicide.

Chapter 3

Methods and Materials

This chapter presents an overview of the methods, materials, formulas and programs used during this thesis.

3.1 Statistical expressions

In the following chapters a variety of standard deviations will be used. While all of them are calculated as normal standard deviations for a sample, the data sets on which they are based differ. Standard deviations will be normed on the median of the underlying dataset and given in percent for better comparability.

3.1.1 Total standard deviation

Total standard deviation refers to the standard deviation over all measurement points within a group. It includes all systematic and random variations that occur.

3.1.2 Run-to-Run standard deviation

The Run-to-Run standard deviation is calculated between the median values of several runs. A run in this case refers to a collection of wafers, that were processed together. As an example, wafers that were implanted directly after each other on the same tool with the same implant conditions belong to the same run, while wafers that were implanted with the same conditions, but at different times or tools, cannot be counted within the same run. This is due to random and systematic variations in the state of the ion implantation tool. Random variations occur when different implant conditions, such as a change in implant species, dose or energy are chosen and the tool needs to recalibrate. Systematic variations can occur, when e.g. the ion source is near the end of its life cycle or a maintenance action was taken. A low Run-to-Run standard deviation denotes smaller changes due to tool variations. A high value of this parameter is an indication that there is a problem.

3.1.3 Wafer-to-Wafer standard deviation

The Wafer-to-Wafer standard deviation is calculated between the median values of all wafers within a single run. It can not be calculated if the run consists of only a single wafer. Since only a single run is the basis for this calculation, only random variations are seen.

3.1.4 Uniformity

The uniformity describes the standard deviation over a single wafer. If the uniformity is given for more than one wafer, it refers to the mean value of the calculated uniformities within a group of wafers.

3.2 Programs

Data analysis was mainly done with Python 3.9 and programs based on the packages numpy 11.22.3 [11], seaborn 0.11.2 [12], pandas 1.4.2 [13], scipy 1.8.0 [14] and matplotlib 3.5.1. [15]. For the simulation of ion implantation profiles for different implant conditions, the software SRIM [16] in the version SRIM-2013.00 was used.

3.3 Materials

The materials and equipment used for all described experiments were provided by Infineon Technologies AG unless explicitly stated otherwise. The experiments were done at the Infineon Technologies sites in Villach and Dresden with the help of the production teams from both sites. Wafers with a diameter of 300 mm and a thickness of 775 μm were provided with two types of base material. The first material was silicon with a resistivity of $40\,\Omega\,cm$ to $145\,\Omega\,cm$, orientation (100) and phosphorous doping in the range of $3.05 \times 10^{13}\,cm^{-3}$ to $1.11 \times 10^{14}\,cm^{-3}$. It will be referred to as n-type Si in later chapters.
The second material was silicon with a resistivity of $10\,\Omega\,cm$ to $26\,\Omega\,cm$, orientation (100) and boron doping in the range of $5.16 \times 10^{14}\,cm^{-3}$ to $1.36 \times 10^{15}\,cm^{-3}$. It will be referred to as p-type Si.

3.4 Sheet resistance measurement

The 4-point-probe is the method used most often to measure the sheet resistance of a material. It uses four equidistant contact probes, that form a line and are brought into contact with the wafer. A current is passed through the outer points of the probe and the voltage drop between the inner points is measured. The resulting sheet resistance R_S is "the ratio of the DC voltage drop per unit length to the surface current per width".[17, p. 89] The resistivity ρ in $\Omega\,cm$ is defined as

$$\rho = \frac{1}{n \cdot e \cdot \mu} \tag{3.1}$$

with $n \ldots$ carrier concentration, electronic charge $e = 1.602 \cdot 10^{-19} C$ and carrier mobility μ. The resistivity does not depend on the geometry of the sample.

The sheet resistance R_S with unit $\Omega/\square$ is given by

$$R_S = \frac{\rho}{d} \tag{3.2}$$

where d is the thickness of the measured sample. This formula assumes a homogeneous distribution of dopants through the entire sample. For the calculation of the sheet resistance following an implant step, the formula needs to account for a non-homogeneous dopant distribution as well as the change in mobility, depending on the dopant concentration. This results in

$$R_S = \frac{1}{\int eN(x)\mu\{N(x)\}dx} \tag{3.3}$$

like it was used by Spangenberg et al.. [18] Assuming a constant dopant concentration within a sufficiently small part δx of the total sample thickness t, the integral can be approximated as

$$R_S = \frac{1}{\sum_i \dfrac{1}{R_{S_i}}} \tag{3.4}$$

where the R_{S_i} are calculated with eq. (3.2). The sheet resistance R_S can be converted to resistance R as follows.

$$R = \rho\frac{l}{A} = \rho\frac{l}{d \cdot w} = R_S \cdot d\frac{l}{d \cdot w} = R_S\frac{l}{w} \tag{3.5}$$

Here w is the width of the sample and l is the distance between the two inner contact points of the four-point-probe setup. The main advantage of using a four-point-probe instead of a two-point-probe is the elimination of the contact resistance and the resulting gain in accuracy. [18, 19] To get a reliable measurement the thickness of the conducting layer must be "less than 40 % of the probe spacing". [17, p. 85] Sheet resistance measurements on unstructured wafers were done with a probe spacing of 0.6 mm. The typical implant profiles reached a depth of approximately 200 nm. The condition for reliable measurements was therefore met.

There are a number of parameters which have an impact on the measured sheet resistance. In the following sections the parameters in the process steps implantation, annealing and measurement, that have the highest impact on the measurement are discussed. The influence of the scattering oxide in terms of thickness or formation process as well as of the various cleaning steps was not examined. While the angle between the beam and the wafer also influences the resulting sheet resistance due to a change in the implant profile, this parameter was not examined during this thesis. Instead a fixed angle of either 7° or 0° was chosen, depending on whether or not the implanted wafer was structured or not.

3.4.1 Implant Parameters

The implant parameters varied for this thesis were the implant dose, energy and beam current. As a reminder, the formula for the sheet resistance is calculated with

$$R_S = \frac{\rho}{t} = \frac{1}{n \cdot e \cdot \mu \cdot t}$$

The implant depth t is controlled by the energy. The mobility μ and the number of dopants n depend on the implanted dose. Assuming a homogeneous distribution of the dopants, the implanted dose in cm^{-2} divided by the implantation depth in cm returns n.

$$n = \frac{Dose}{d} \tag{3.6}$$

Several models for the relationship between μ and n have been proposed. [20, 21, 22, 23, 24, 25] Depending on the model the value for the mobility varies. Most values found in the literature for the mobilities of electrons and holes, μ_e and μ_h, are either based on the formulas (3.7a), (3.7b) from Masetti et. al [20], on (3.8a), (3.8b) from Arora et. al [21] or on models derived from one of them [22].

$$\mu_e = 68.5 + \frac{1414 - 68.5}{1 + \left(\frac{n}{9.2 \times 10^{16}}\right)^{0.711}} - \frac{56.1}{1 + \left(\frac{3.41 \times 10^{20}}{n}\right)^{1.98}} \tag{3.7a}$$

$$\mu_h = 44.9 e^{\frac{-9.23 \times 10^{16}}{n}} + \frac{470.5}{1 + \left(\frac{n}{2.23 \times 10^{17}}\right)^{0.719}} - \frac{29}{1 + \left(\frac{6.1 \times 10^{20}}{n}\right)^{2.00}} \tag{3.7b}$$

Equation (3.7a) is valid for room temperature and phosphorous doping in a range of $10^{13}\,\text{cm}^{-3}$ to $5 \times 10^{21}\,\text{cm}^{-3}$, while eq. (3.7b) is valid for boron doping in the range of $10^{14}\,\text{cm}^{-3}$ to $1.2 \times 10^{21}\,\text{cm}^{-3}$.

$$\mu_e = 88 \cdot \left(\frac{T}{300}\right)^{-0.57} + \frac{7.4 \times 10^8 \cdot T^{-2.33}}{1 + 0.88 \left[\frac{N_d}{1.26 \times 10^{17}\left(\frac{T}{300}\right)^{2.4}}\right]\left(\frac{T}{300}\right)^{-0.146}} \tag{3.8a}$$

$$\mu_h = 54.3 \cdot \left(\frac{T}{300}\right)^{-0.57} + \frac{1.36 \times 10^8 \cdot T^{-2.23}}{1 + 0.88 \left[\frac{N}{2.35 \times 10^{17}\left(\frac{T}{300}\right)^{2.4}}\right]\left(\frac{T}{300}\right)^{-0.146}} \tag{3.8b}$$

The formulas (3.8a), (3.8b) given by Arora et. al are valid for temperatures between $250\,\text{K}$ to $500\,\text{K}$ and dopant concentrations in the range of $10^{13}\,\text{cm}^{-3}$ to $10^{20}\,\text{cm}^{-3}$. Where necessary, calculations were done with the resulting mobilities from both sets of formulas.

3.4.2 Base Material

The dopant concentration of the base material has an influence on the measured sheet resistance. It depends on the dopant concentrations of the base material and of the implanted species. As stated in [26] the implanted species and the base material are usually of opposite type, meaning that a p-type implant should be combined with a n-type substrate and vice versa. This has the advantage of a pn-junction as an isolating measure between the implanted area and the rest of the substrate material. It also results in a partial neutralisation of the implanted dose with the dopants of the base material. For optimal monitoring conditions, the dopant concentration of the base material should therefore be as stable as possible between different samples and several orders of magnitude below the concentration of the implanted species. Under the assumption of a uniform dopant distribution for the base material and the implanted layer, "the amount of the implanted dosage which is neutralized and depleted in a unit area D_{del}, can be approximated as:"[26]

$$D_{del} = D_s t + 3.64 \times 10^3 \sqrt{(D_i - D_s t) \frac{D_s}{D_i}} \qquad (3.9)$$

where the substrate doping density D_s is given in cm^{-3}, the implanted dose D_i is given in cm^{-2} and the layer thickness t is given in cm.

3.4.3 Anneal

The Anneal following the implantation is used to heal crystal damage caused by the implantation and to electrically activate the dopant atoms. Dopant atoms implanted into the material are incorporated into the silicon lattice as substitutional atoms.[27]

3.4.4 Four-Point Probe Measurement Tool

The sheet resistance measurement for unstructured wafers was done with a four-point measurement on Omnimap RS200 measurement tools. All sheet resistance measurements for this thesis were done at room temperature, with either 49 or 441 measurement points. The number of measurement points was mainly a factor in determining the uniformity across the wafer. The needles used to contact the wafers were monitored and replaced regularly to eliminate contact issues. Each needle was pressed to the wafer surface with 100 g.

3.4.5 Sensitivity

A point that must not be overlooked is the sensitivity of the measurement on certain changes in parameter values. As stated by Hamby, "the simplest approach to sensitivity analysis is the one-at-a-time method"[28], where the parameters influencing the output are varied separately. Hamby also mentions that this method is also known as "'local' sensitivity analysis" [28], due to it's dependence on the base case. Therefore, the analysis needs to be repeated for every change of the base case.[28]

During the course of this thesis, local sensitivity analysis was performed to evaluate the influence of the parameters described above. The method was chosen over other possible

Table 3.1: Maximum Deviations possible for each process step in section 3.5

Parameter	max. Deviation	Unit
Counter Dose	3	%
Annealing Time	1	s
Annealing Temperature	3	°C
Energy	1	keV
Base Material	14	%

sensitivity analysis techniques, since the final process should be fixed with only small changes in parameter values, therefore providing a stable base case.

To evaluate the sensitivity, wafers were implanted with the procedure specified in section 3.5, while varying the process parameters. Sensitivities were calculated under the assumption of linearity in case of small variations with formula (3.10)[28].

$$S = \frac{\triangle Y\,[\%]}{\triangle X_i\,[\%]} \tag{3.10}$$

In eq. (3.10) $\triangle Y\,[\%]$ is the observed change after a small implemented change of parameter X. Both are given in %.

For the ease of comparison sensitivity values will be given with regard to percentages. As an example, the sensitivity of the sheet resistance on a change in the implanted dose is then given by $dR_S[\%]/dD[\%]$. For exceptions the units will be explicitly mentioned.

3.4.6 Repeatability

The sheet resistance measurement method is further characterised by its repeatability. Repeatability is defined as the variation between measurements taken with the same measurement system, by the same operator, on the same sample under the same conditions. It is used in combination with the sensitivity to determine if a measurement system or method is capable of measuring a certain variable. [29]

As stated by Smets et. al [30] the calculated sensitivities S_i, in combination with their expected standard deviations σ_i and the measurement repeatability can be used to approximate the total expected variance for a measurement with formula

$$\sigma_{tot}^2 = S_{dose}^2 \cdot \sigma_{dose}^2 + \sum_i S_i^2 \cdot \sigma_i^2 + \sigma_{repeatability}^2 \tag{3.11}$$

The maximum deviations for each process in section 3.5 can be taken from table 3.1.

In accordance with [29], the gage capability of a measurement can then be calculated with eq. (3.12), where *Range* is the tolerance range for the whole process. For the sheet resistance measurements on unstructured wafers this range is assumed to be 60.

$$GRR\% = \frac{6\sigma_{tot}}{Range} \tag{3.12}$$

3.5 General Processflow for unstructured wafers

The experiments on unstructured wafers followed the general processflow depicted in fig. 3.1. Wafers were cleaned with Standard Clean 1 (NH4OH/H2O2/H2O) and Standard Clean 2 (HCl/H2O2/H2O). A 30 nm thick SiO2 layer was deposited to avoid channeling during the ion implantation. After the ion implantation the wafers were again cleaned with Standard Clean 1 and Standard Clean 2 and annealed in a Rapid Thermal Annealing (RTP) process. Following an oxide removal step with a 10 % HF solution and a cleaning step with Standard Clean 1 and 2, the wafer was measured with a 4-point-probe on 441 measurement sites. The resulting values allowed conclusions to be drawn about the dose. As a base case for this processflow a dose of $1.5 \times 10^{14}\,\mathrm{cm^{-2}}$ implanted with an energy of
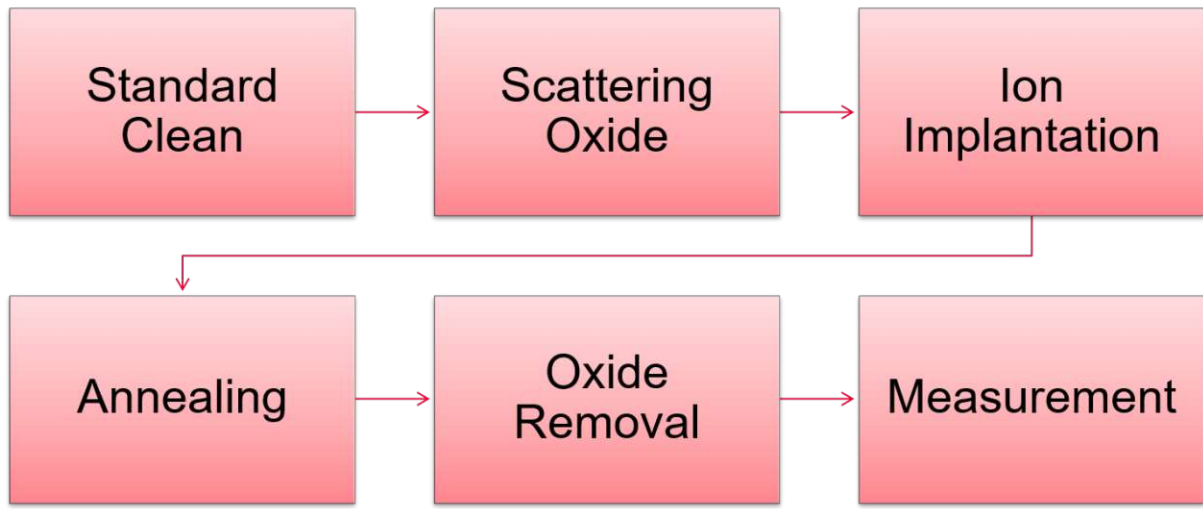
Figure 3.1: General process flow used for experiments on
unstructured wafers

45 keV at an angle of 7° and annealed with a temperature of 1040 °C for a duration of 30s was chosen.

The plausibility of the measurement results was checked trough the simulation of the implantation profile with the software SRIM in the version SRIM-2013.00. The implantation profiles for a given set of implant conditions were extracted and the sheet resistance was calculated with equations 3.2 and 3.4, with a δx of 1 nm. The mobility for each R_{S_i} was calculated with eqs. (3.7a), (3.7b), (3.8a) and (3.8b).

3.6 Theoretical background for multiple implants

Based on the rules for the calculation of the variance of a sample, the variance of the implanted dose X depending on the number of implant steps n is given by equation 3.13.

$$Var\left(\frac{1}{n}\sum_{i=1}^{n}X_i\right) = \frac{1}{n^2}\left(\sum_{i=1}^{n}Var\left(X_i\right)\right) = \frac{n \cdot \sigma^2}{n^2} = \frac{\sigma^2}{n} \tag{3.13}$$

The resulting standard deviation is then given by

$$\sigma_{\frac{1}{n}\sum_{i=1}^{n}X_i} = \frac{\sigma_X}{\sqrt{n}} \tag{3.14}$$

Therefore the standard deviation for a single implanted dose should be higher than the deviation for 10 implant steps with $^1/_{10}$ of the dose by a factor of $\sqrt{10}$. This reduction of random variations enables a better identification of systematic variations. While this reduction is visible for all 4 variations outlined in section 3.1, it is most noticeable for Run-to-Run variations.

3.7 Low Energy Ion Scattering

Low Energy Ion Scattering (LEIS) was used to analyse the surface of unstructured wafers in regard to its atomic composition. LEIS measurements were performed as an external measurement by the Center of Electrochemical and Surface Technology (CEST) in Wiener Neustadt.

The technique uses noble gas ions and energies below $8\,\mathrm{eV}$ to probe a sample from the first monolayer to a depth of up to $10\,\mathrm{nm}$ and is not influenced by matrix effects. Ions of mass m_1 with starting energy E_0 are scattered by the sample atoms of mass m_2 and their final energy E_f after the scattering processes is measured by a detector typically fixed under an angle Θ.

$$E_f = \left(\frac{cos\Theta + \sqrt{\left(\frac{m_2}{m_1}\right)^2 - sin^2\Theta}}{1 + \frac{m_2}{m_1}} \right)^2 \cdot E_0 \tag{3.15}$$

Equation (3.15) [31, p. 419] describes the relationship between E_0 and E_f. Since m_1, E_0 and Θ are fixed and E_f is measured, the only unknown is m_2, which can be calculated by transforming eq. (3.15).

It must be noted, that only a fraction of the incident ions N_P contribute to the measured signal from the first monolayer. The efficiency of the detector, surface roughness, scattering cross section, probability of primary ions remaining ionised and the atomic concentration of the surface elements reduce the measured signal by a factor of 1×10^{-7} compared to N_P. The main part of the other ions reach greater depths of the sample and are scattered there and have to be reionized as they leave the sample again to contribute to the signal as low energy tails of the surface scattering peaks, where the tail width indicates the depth distribution and the height indicates the concentration of an element in the sample. The rest of the primary ions do not reach the detector.

Different cleaning techniques may be used to prepare the sample. Typical results are plotted as a function of the signal intensity given in counts/nC, which describes "the measurement signal normalized to the number of primary ions used"[31, p. 424], to allow an easier comparison between spectra recorded under different conditions. [31, pp. 419-424]

The LEIS results described in section 6.3 were measured on an ION-TOF Qtac[100] high sensitivity LEIS spectrometer with a primary beam of Helium ions with $3\,\mathrm{keV}$ and a current of $2.05\,\mathrm{nA}$ to $2.14\,\mathrm{nA}$. A Faraday Cup was used to measure the current. The incident angle was $0°$ and the scattering angle Θ was $145°$. The measurement area was $2 \times 2\,\mathrm{mm}^2$.

Sputtering was done with Argon ions at $500\,\text{eV}$, a current of $100\,\text{nA}$, $59°$ incident angle, for $40\,\text{s}$ over an area of $2.5 \times 2.5\,\text{mm}^2$.

3.8 Vapor Phase Decomposition

Vapor Phase Decomposition (VPD) was used in combination with Inductively Coupled Plasma Mass Spectroscopy (ICP-MS) to further analyse the impurities on the surface of unstructured wafers. During the VPD wafers with a native oxide are exposed to HF vapor. The native oxide is etched by the HF and the resulting water droplet containing the impurities that were on or in the oxide is then collected. The collected droplet is analysed with the ICP-MS. It is "nebulized and ionized in an inductively coupled plasma. Once in ion form, the ions are analyzed in a mass spectrometer, most commonly a quadrupole mass spectrometer"[32, p.667]

3.9 Total X-Ray Fluorescence Spectrometry

Total X-Ray Fluorescence Spectrometry (TXRF) can be used to determine contaminants on a wafer surface. Monochromatic x-rays hit the wafer at an angle below the limiting angle of the total reflection and are used to excite electrons in the lower shells of the target material atoms. Their previous state is then filled by an electron from a higher shell, that emits radiation characteristic for the energy difference between the involved shells. Through this the elements on the wafer surface can be determined. [33]

TXRF measurements for this thesis were performed under clean room conditions with a Rigaku 310V with $35\,\text{keV}$, $255\,\text{mA}$. 277 points were measured per wafer.

Chapter 4

Unstructured Wafers

This chapter concerns experiments done on unstructured or blank wafers, that were subjected to single or multiple implants and various annealing conditions. Some wafers were implanted multiple times with low doses instead of a single implant with a high dose. The intention was to reduce the standard deviation through the use of statistical effects. For a few wafers an additional, slightly deeper implant of the opposite doping type was made to create a pn-junction under the first implant to be measured. This was done to suppress parasitic contributions from the bulk to the four-point measurement, in cases where the bulk doping was of the same type as the implant. In such cases the additional implant will be referred to as a counter implant, while the implant that is to be measured will be called active implant.

4.1 Sensitivity

To evaluate the sensitivity of the sheet resistance measurement on influences from the process flow on the base case described above, local sensitivity analysis was performed as described in section 3.4.5. The parameters used for this analysis were the dopant concentration within the base material, the thickness of the scattering oxide, implant dose and energy of the active and counter implant, annealing temperature and annealing time. As seen in table 4.1 the implanted dose showed the highest impact on the sheet resistance. As a result the implanted dose was chosen as the defining feature of the base case and multiple local sensitivities were calculated.

4.1.1 Annealing

Figure 4.1 shows the results of an RTP parameter split experiment for phosphorus implanted wafers. 12 Wafers were preprocessed according to 3.5 and implanted with $1.5 \times 10^{14}\,\mathrm{cm^{-2}}$ phosphorus at $115\,\mathrm{keV}$ and with a $1.5 \times 10^{13}\,\mathrm{cm^{-2}}$ boron counter implant at $150\,\mathrm{keV}$. Each wafer saw different annealing conditions. Wafers were annealed at $1000\,^{\circ}\mathrm{C}$, $1040\,^{\circ}\mathrm{C}$, $1050\,^{\circ}\mathrm{C}$, $1100\,^{\circ}\mathrm{C}$, with one wafer per temperature at times of $30\,\mathrm{s}$, $60\,\mathrm{s}$ and $90\,\mathrm{s}$. As seen in fig. 4.1 the base case parameters $1040\,^{\circ}\mathrm{C}$ and $30\,\mathrm{s}$ resulted in the lowest sheet resistance among the split groups. Wafers annealed at temperatures $\leq 1040\,^{\circ}\mathrm{C}$ show increasing sheet resistance with increasing time. For wafers annealed at $1050\,^{\circ}\mathrm{C}$ and $1100\,^{\circ}\mathrm{C}$ the

22

Parameter	Boron	Phosphorous
Substrate Doping Concentration	-0.0040	-0.0020
Scattering Oxide	0.053	0.053
Dose	-0.7492	-0.6749
Energy	-0.5817	-0.2401
Anneal Temperature	-0.0038	0.0044
Anneal Time	-0.0094	-0.0085
Parameter	Repeatability: Boron	Repeatability: Phosphorous
R_S measurement	0.1130	0.6538

Table 4.1: Sensitivity values for the critical parameters. The values were calculated as described in section 3.4.5 with data from experiments in section 4.1.1, section 4.1.2 and section 4.1.3 for the base case of $1.5 \times 10^{14}\,\mathrm{cm^{-2}}$

.

sheet resistance decreased with increasing time. It is notable, that the median values are close to $372\,\Omega/\square$ for the shortest time and increase toward $375\,\Omega/\square$ for low temperature annealings. For high temperature annealings the opposite behaviour was observed.

To evaluate the influence of the annealing parameters on the sheet resistance of boron implanted wafers, 9 wafers were preprocessed following the general process flow for unstructured wafers with the base case values for boron implantation. At the RTP process, wafers were annealed with $1020\,^{\circ}\mathrm{C}$, $1040\,^{\circ}\mathrm{C}$ and $1060\,^{\circ}\mathrm{C}$. For each temperature a wafer was annealed for a duration of $15\,\mathrm{s}$, $30\,\mathrm{s}$ or $60\,\mathrm{s}$. After the anneal, the wafers were stripped of the scattering oxide following the general process flow and measured.
The resulting sensitivities with regard to annealing time and temperature can be taken from table 4.1.
Figure 4.2 shows the sheet resistance values for the different annealing conditions. It is evident, that longer annealing times lead to a slight decrease in sheet resistance, but the very low sensitivity values indicate small variations of the considered annealing temperature and time do not significantly effect the sheet resistance.

4.1.2 Dose

A dose split was performed for As and P into p-type Si with $250\,\mathrm{keV}$ and $115\,\mathrm{keV}$ respectively. Another dose split was done for B with $45\,\mathrm{keV}$ into n-type Si. P and B were implanted under an angle of $7°$ and As under $0°$. The energies were chosen to create implant profiles with similar depths. All other processes were performed as described in section 3.5. The implant doses and the medians of the resulting sheet resistances per wafer, along with their respective standard deviations are given in table 4.2. P and As show similar values for the sheet resistances for all 5 doses, but the standard deviations for P are slightly higher. B shows higher sheet resistances, but lower standard deviations compared to As and P for all doses. Qualitatively the sheet resistances become lower the higher the implant doses are, as is expected for all three species.
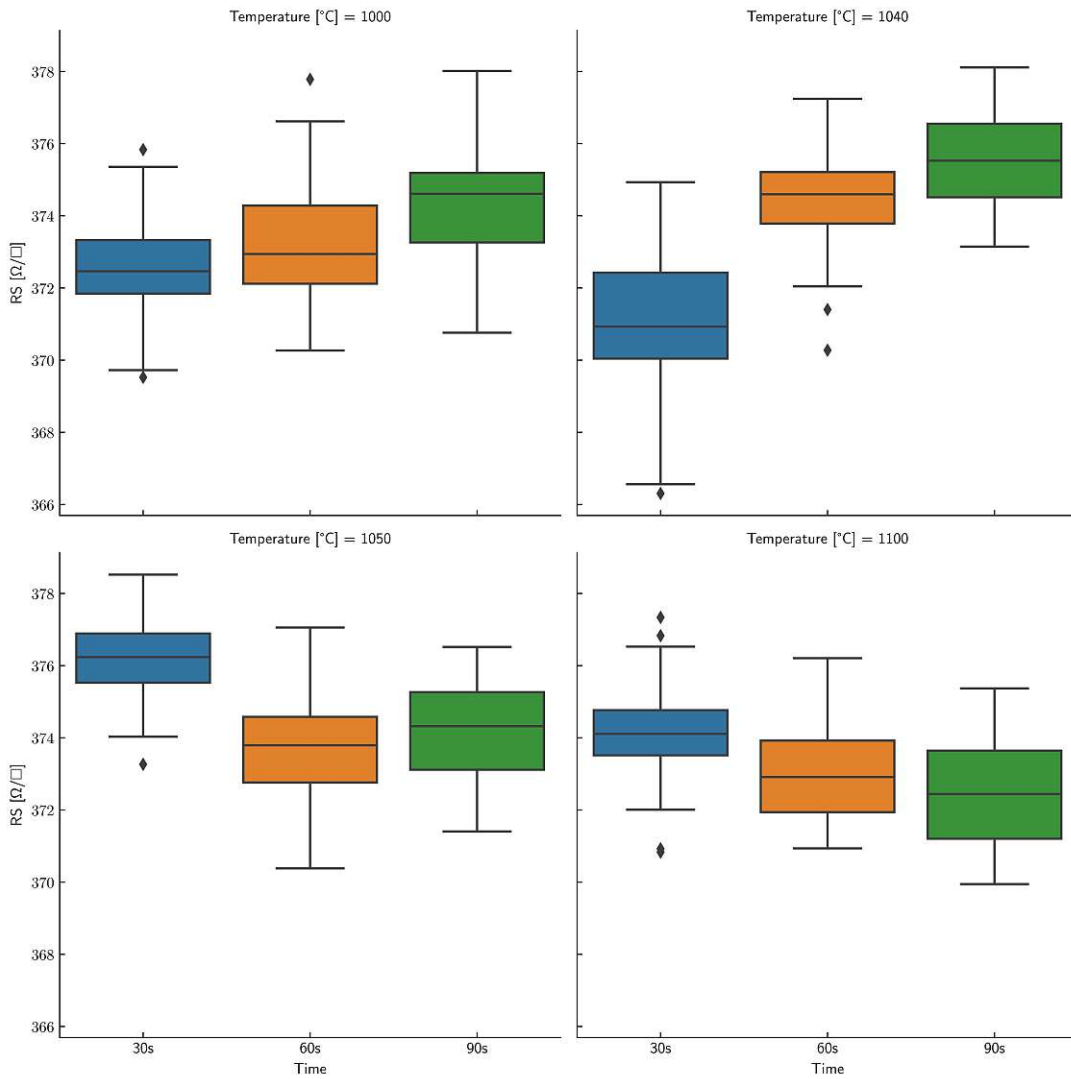
Figure 4.1: RS values of RTP parameter split experiment, grouped by annealing time and temperature for phosphorus ion implantation.

Figure 4.3 shows, that the relationship between the sheet resistance and the implanted dose can be described by the following power law,

$$RS = e^b \cdot D^a \tag{4.1}$$

with the sheet resistance RS in $\Omega/\square$ and the implanted dose D in cm^{-2}. The parameters a and b can be determined by a fit of the linearised form of eq. (4.1).

$$log(RS) = a \cdot log(D) + b \tag{4.2}$$

The results of the fits are shown in fig. 4.3 and the fit parameters can be taken from table 4.3. For arsenic and phosphorous the fit parameters are similar. The fit for boron resulted in a slightly lower a and higher b value, but still in the same order of magnitude, indicating, that the qualitative behaviour is comparable, even if the absolute values differ. For arsenic and phosphorous the sheet resistance values as well as the dose dependency of the sheet resistance are very similar resulting in nearly congruent fits. For boron

24

Table 4.2: The definition of splitgroups and process conditions for dose split and the resulting median resistance values per group with their respective standard deviations are given.

Species	Dose [cm^{-2}]	Median R [$\Omega/\square$]	Stdv [%]
As	1.5×10^{13}	1079.43	0.3738
As	3.0×10^{13}	749.48	0.3739
As	7.5×10^{13}	485.888	0.2886
As	1.5×10^{14}	333.419	0.2375
As	3.0×10^{14}	208.134	0.1788
P	1.5×10^{13}	1131	0.4389
P	3.0×10^{13}	765.720	0.3202
P	7.5×10^{13}	475.173	0.3730
P	1.5×10^{14}	319.555	0.2962
P	3.0×10^{14}	202.11	0.2479
B	1.5×10^{13}	2502.62	0.2235
B	3.0×10^{13}	1528.68	0.1788
B	7.5×10^{13}	817.874	0.2925
B	1.5×10^{14}	498.755	0.1976
B	3.0×10^{14}	289.243	0.2205

Table 4.3: Fit Parameter calculated for arsenic, phosphorous and boron

Species	a	b
As	-0.538	23.334
P	-0.567	24.249
B	-0.714	29.51

25
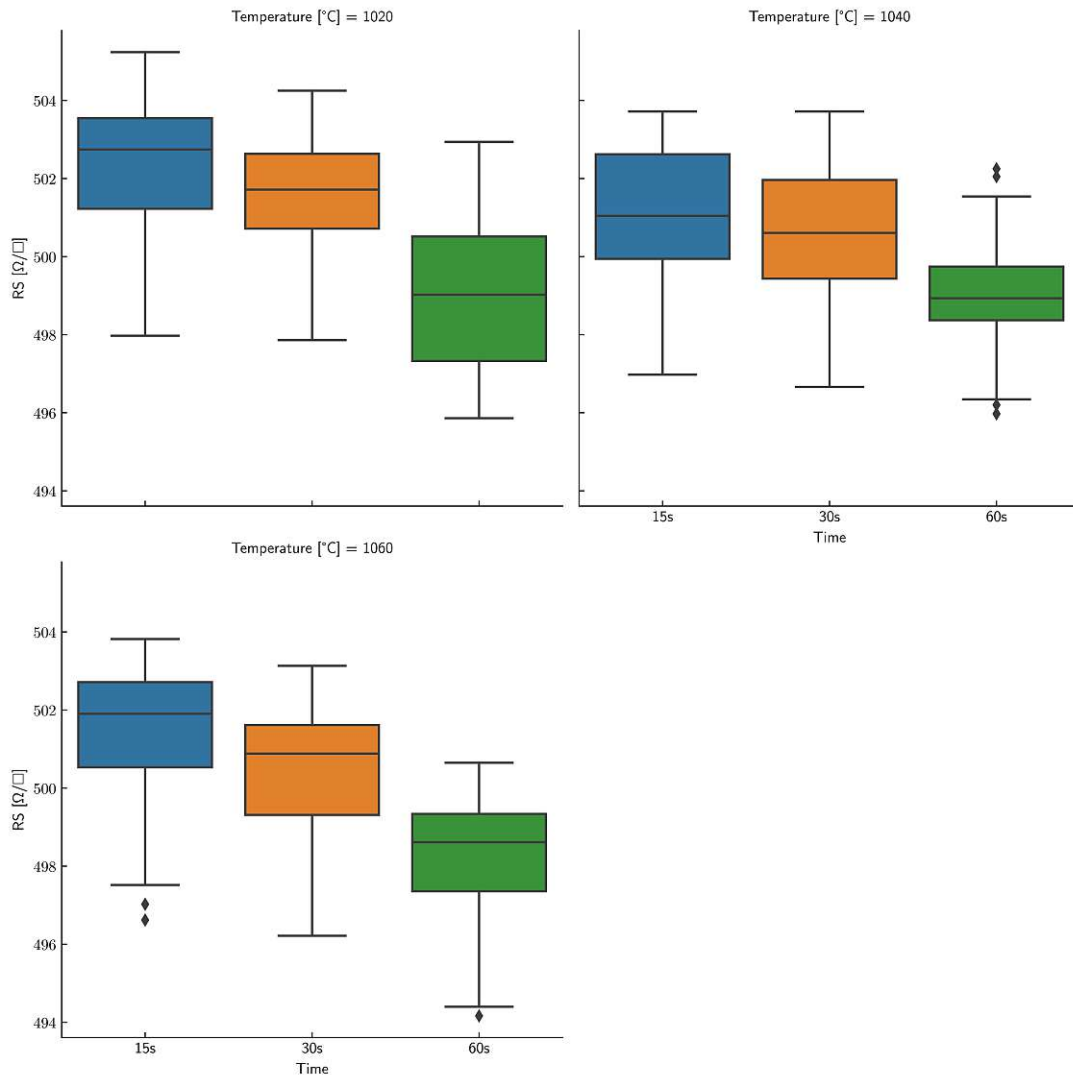
Figure 4.2: RS values of RTP parameter split experiment, grouped by annealing time and temperature for boron ion implantation.

higher sheet resistance values were observed with a higher dose dependency indicated by a steeper slope compared to arsenic and phosphorous. The observed dependency of the sheet resistance for boron of $a \cong -0.71$ is in good agreement with the -0.73 reported for implantation with BF2 in [34].

Through the fit function it is possible to calculate the sensitivities of the sheet resistance on the implanted dose for all 5 doses. It is assumed, that the sensitivity is linear for small changes in dose, as it was described in section 3.4.5. With this the sensitivity can be calculated as either the first derivative of eq. (4.1) at a dose D or through the use of eq. (3.10) with a dose variation of $\pm 1\,\%$ of the current dose D. Both methods are in good agreement with each other up to the fourth decimal place. The exact values normed on the resistance and dose can be taken from table 4.4. The values apply to all 5 used implant doses, due to the normalisation. Arsenic and phosphorus show similar sensitivity values, boron shows a slightly higher sensitivity.
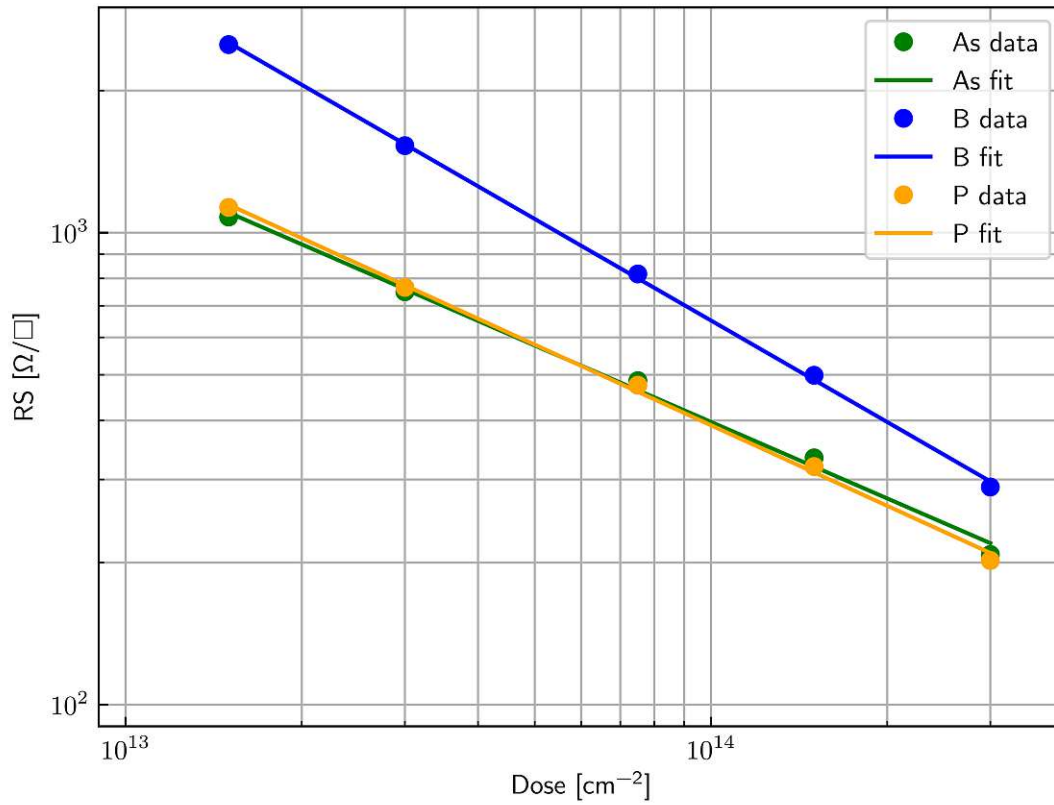
Figure 4.3: Median sheet resistances over implant dose with
log-log scales and fit

4.1.3 Energy

The energy chosen for the ion implantation changes the depth distribution of the implanted ions. Through this it effects the measured sheet resistance. 3 wafers were processed with the general process flow and implanted with $1.5 \times 10^{14}\,\mathrm{cm}^{-2}$ boron at $40\,\mathrm{keV}$, $45\,\mathrm{keV}$ and $50\,\mathrm{keV}$ respectively. The median sheet resistance values for these wafers were $516.767\,\Omega/\square$, $502.081\,\Omega/\square$ and $487.560\,\Omega/\square$. They are in good agreement with the theoretical values calculated with eq. (3.7b) and the SRIM profiles for the above mentioned conditions. The theoretical values calculated with 3.8b overestimated the measured values drastically. Figure 4.4a shows the simulated depth profiles for ion implantation with these conditions. For higher energies the peak is located deeper in the substrate and shows a lower concentration of ions, due to a a broadening of the profile.

Table 4.4: Sensitivity values $^{dR[\%]}/_{dD[\%]}$ for As, B and P in the
dose range $1.5 \times 10^{13}\,\mathrm{cm}^{-2}$ to $3.0 \times 10^{14}\,\mathrm{cm}^{-2}$ calculated with the
derivative of the fit and with the linear dose variation

Species	Derivative	Dose variation
As	-0.538	-0.538
B	-0.714	-0.714
P	-0.567	-0.567

It was assumed, that the change in sheet resistance is linear in the considered energy range. This resulted in a sheet resistance change of $-0.58\,\%$ for a deviation of $1\,\text{keV}$ from the base case energy.

The process was repeated with 3 wafers for a boron dose of $1.5 \times 10^{13}\,\text{cm}^{-2}$. For this dose the theoretical values calculated with the mobilities from eq. (3.8b) offered a better approximation of the measured sheet resistances. With the measured values $2604.516\,\Omega/\square$, $2490.4301\,\Omega/\square$ and $2407.519\,\Omega/\square$ for $40\,\text{keV}$, $45\,\text{keV}$ and $50\,\text{keV}$ a sheet resistance change of $-0.7877\,\%$ for a deviation of $1\,\text{keV}$ from the base case energy was calculated.

(a) Boron   (b) Phosphorous
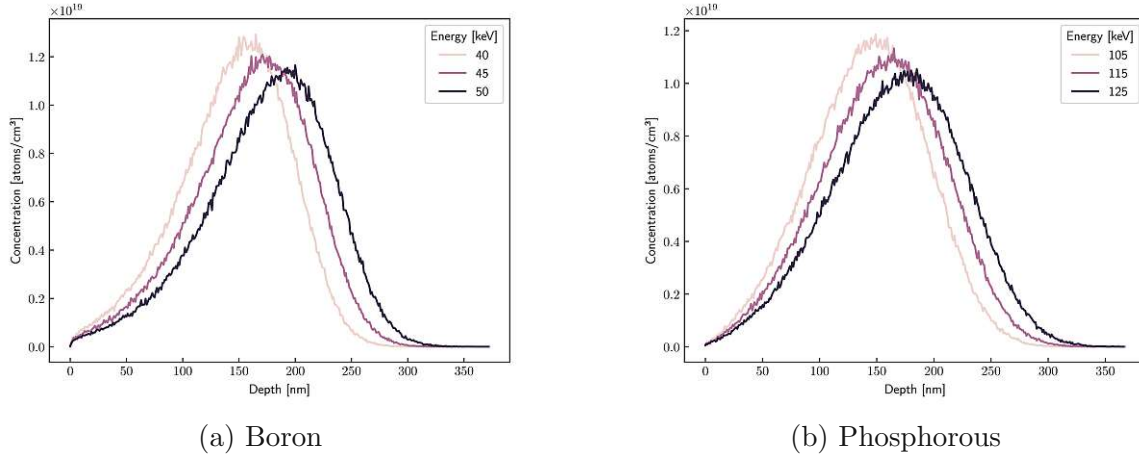
Figure 4.4: Depth profiles of boron and phosphorous implantation into Si with $1.5 \times 10^{14}\,\text{cm}^{-2}$ at different energies simulated with SRIM.

The sensitivity on implantation energy changes was also evaluated for phosphorus implants. Wafers were implanted with a phosphorus dose of $1.5 \times 10^{14}\,\text{cm}^{-2}$ at $105\,\text{keV}$, $115\,\text{keV}$ and $125\,\text{keV}$. A counter implant with $1.5 \times 10^{13}\,\text{cm}^{-2}$ boron at $150\,\text{keV}$ was used. In fig. 4.4b the dopant depth distributions for these implant conditions are plotted. The median measured sheet resistances were $386.514\,\Omega/\square$, $376.621\,\Omega/\square$ and $368.402\,\Omega/\square$. Theoretical values were calculated for comparison with eq. (3.7a) and eq. (3.8a). The depth profiles of the ion concentrations were simulated with SRIM and the Concentration of the counter implant was deducted from the concentration of the active implant concentration. While the calculated values were consistently below the measured ones for both mobility variations, all three showed a reduction in sheet resistance with increasing energies. The value for the sensitivity can be taken from table 4.1.

4.1.4 Scattering Oxide

To evaluate the influence of the scattering oxide on the measured sheet resistance, 9 wafers were processed according to section 3.5, but with differing oxide thickness. Three wafers each were processed with the standard thickness of $30\,\text{nm}$, $-10\,\%$ and $+10\,\%$ of the standard thickness. The mean of the measured oxide thicknesses for the three groups were $31\,\text{nm}$, $28\,\text{nm}$ and $34.5\,\text{nm}$. Over the course of 9 days the wafers were implanted, annealed and measured. The measured sheet resistances resulted in mean values of $497.23\,\Omega/\square$, $493.27\,\Omega/\square$ and $500.27\,\Omega/\square$ for $30\,\text{nm}$, $-10\,\%$ and $+10\,\%$ respectively. Through the use of section 3.4.5 the sensitivity was calculated to be 0.053, when the measured change in the

Table 4.5: Implant conditions and results for Gauge Study:

Base Material	Species	Dose [cm^{-2}]	Energy [keV]	max. Stdev [$\Omega/\square$]	max. Stdev [%]	max. Difference [$\Omega/\square$]
n-type Si	B	1.5E14	45	0.4640	0.0919	1.11
n-type Si	B	5x3.0E13	45	0.4236	0.0844	0.99
n-type Si	P	5x3.0E13	115	0.7002	0.1833	1.54
p-type Si	P	1.5E14	115	0.378	0.118	0.978
p-type Si	As	1.5E14	250	0.247	0.074	0.595

sheet resistance and the implemented change of the scattering oxide thickness are given in percent.

4.2 Repeatability

The repeatability of the four-point measurement was checked with 3 n-type Si and 2 p-type Si wafers. The wafers were implanted, annealed and cleaned as stated in section 3.5. Each wafer was measured 5 times in a span of 40 min with 49 measurement points. The measured values for each point and wafer were analysed in terms of maximum difference and standard deviation between measurements. The implant species and conditions, as well as the calculated results can be taken from table 4.5. The different energies are due to the differences in implantation depths of the species. The energies were chosen according to SRIM simulations to make the depth distributions of the dopants as similar as possible. While the wafer implanted with phosphorus in a dose of 5x3.0E13, shows the highest maximum standard deviation between measurement points, as well as the highest maximum difference, it has to be taken into account, that this wafer saw a second implant to create the pn-junction necessary for the measurement.

4.3 Multiple Implants

Experiments with multiple implant steps were performed on wafers with both p-type Si and n-type Si base materials.

4.3.1 5x, 10x, 15x Implants

The wafer processing followed the steps outlined in section 3.5, with one difference. The implanted dose of $1.5 \times 10^{14}\,\text{cm}^{-2}$ was split into multiple smaller implant doses, that were implanted one after the other, with a waiting period of approximately 2 days in between. The waiting period varied due to variations in the availability of the ion implantation tools.

The exact implant doses used can be taken from table 4.6. The wafers were processed in groups of 5, with one wafer from each splitgroup. Splitgroups 1 to 4 saw boron implants with 1, 5, 10 and 15 implant steps with their respective doses. The fifth splitgroup saw a boron counter implant of $1.5 \times 10^{13}\,\text{cm}^{-2}$ with an energy of 150 keV, placing it below

Table 4.6: Number of implant steps needed for a total dose of $1.5 \times 10^{14}\,\mathrm{cm}^{-2}$

Dose [cm^{-2}]	Implant Steps
1.5×10^{14}	1
3.0×10^{13}	5
1.5×10^{13}	10
1.0×10^{13}	15

the active implant. For this group, the active implant was phosphorus with 15 implant steps. Due to the differences in species, energy and dose, the ion implanter was forced to recalibrate between each implant.

(a) Measured Resistance

(b) Dose Offset

(c) Standard deviations

(d) Run-to-Run
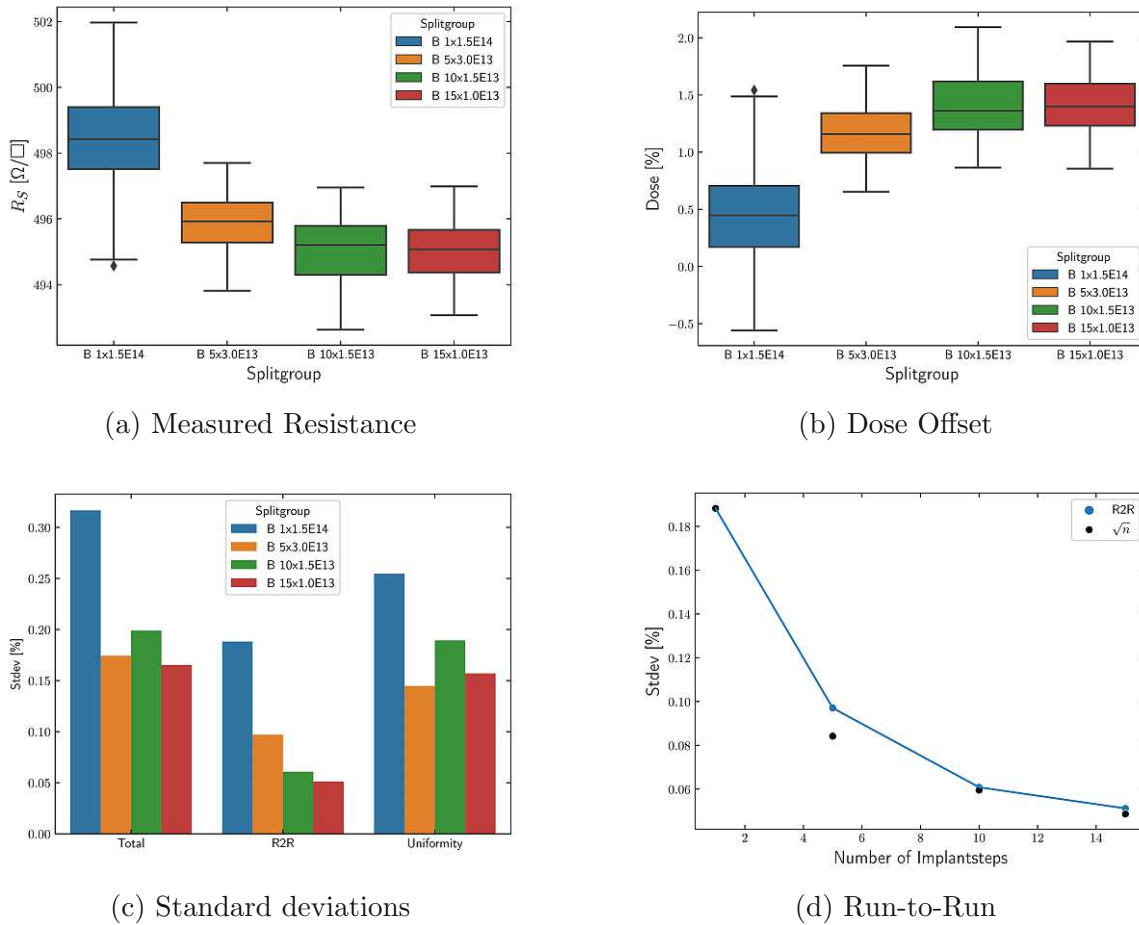
Figure 4.5: Analysis of the splitgroups with multiple boron implants.

Figure 4.5a shows the measured resistance for the boron implanted wafers. Under the chosen implant conditions, a sheet resistance of $500\,\Omega/\square$ is expected. For the single implant wafers the mean of the measured sheet resistance was $498.43\,\Omega/\square$, corresponding to the slight overdose of approximately $0.5\,\%$, depicted in fig. 4.5b. The splitgroups with 5, 10 and 15 implant steps showed a reduced sheet resistance and an overdose around $1.4\,\%$. Figure 4.5c shows the Total, Run-to-Run and Uniformity standard deviations. All three

standard deviations are reduced with multiple implant steps. The Run-to-Run deviation also shows the expected reduction with the square-root of the number of implant steps for 10 and 15 steps. For 5 implant steps the reduction is in the range of the expected value, but does not reach it. 4.5d shows the Run-to-Run values compared to the $R2R(1)/\sqrt{n}$, where $R2R(1)$ is the Run-to-Run value for the splitgroup B 1x1.5E14. An attempt was made to recreate this averaging effect by raising the number of passes that the beam makes over the wafer during an implantation process from 24 to 52. The increase was achieved through a reduction of the beam current and showed no significant improvement of the standard deviations.

4.3.2 Comparison of Multi and Single Implants over Time

Over the course of 4 months unstructured wafers from 3 splitgroups were measured. Splitgroup "Single Implant with STROX" was processed according to section 3.5 under base case conditions. Splitgroup "Single Implant without STROX" was processed similar to the first group, but without a scattering oxide. To avoid channeling wafers were twisted by 23° and the implant energy was reduced to 30 keV. Splitgroup "Multi Implant without STROX" was processed identical to "Single Implant without STROX" with the exception, that the implant dose was implanted in 5 implant steps instead of the single implant that was used for the other two groups. Between the implant steps a wait period of 2 h was added. During this time other wafers were implanted under various conditions to ensure, that the implanter had to retune multiple times until the next implant step. Each wafer saw only one of the ion implantation tools. For this experiment the implanters A, B and C were used. The wafers were scrapped after the measurement.

Figure 4.6 shows the percentage distance of the measured sheet resistance values from the median of all measured values from wafers, that were implanted on the same tool and belong to the same splitgroup. All 3 splitgroups remain within ±1 % at all times in the selected time frame.

As seen in fig. 4.7 the Run-to-Run standard deviations for implanter A and B for the Multi-Implant splitgroup are lower than for the Single Implant with STROX group. For implanter B the Multi Implant without STROX group shows a lower deviation than the Single Implant without STROX. Implanter A showed the reverse behaviour, but with a smaller difference between the groups. For splitgroup Single Implant with STROX B and C were very close. A showed the highest Run-to-Run variation within that group. When the Run-to-Run variation is calculated for a slpitgroup without regard for the used ion implanter, the Single Implant without STROX group reaches a deviation of 0.444 % and the Multi Implant reaches 0.375 %.
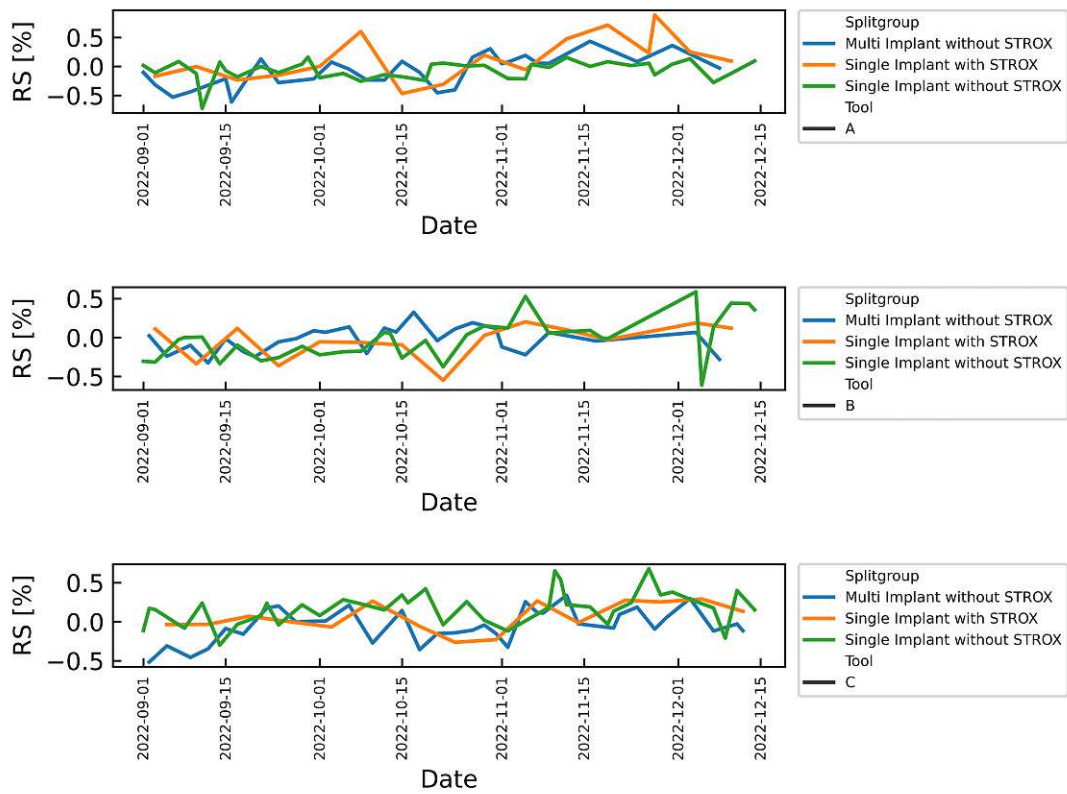
Figure 4.6: Trend of percentage distance to the median for all tools and splitgroups
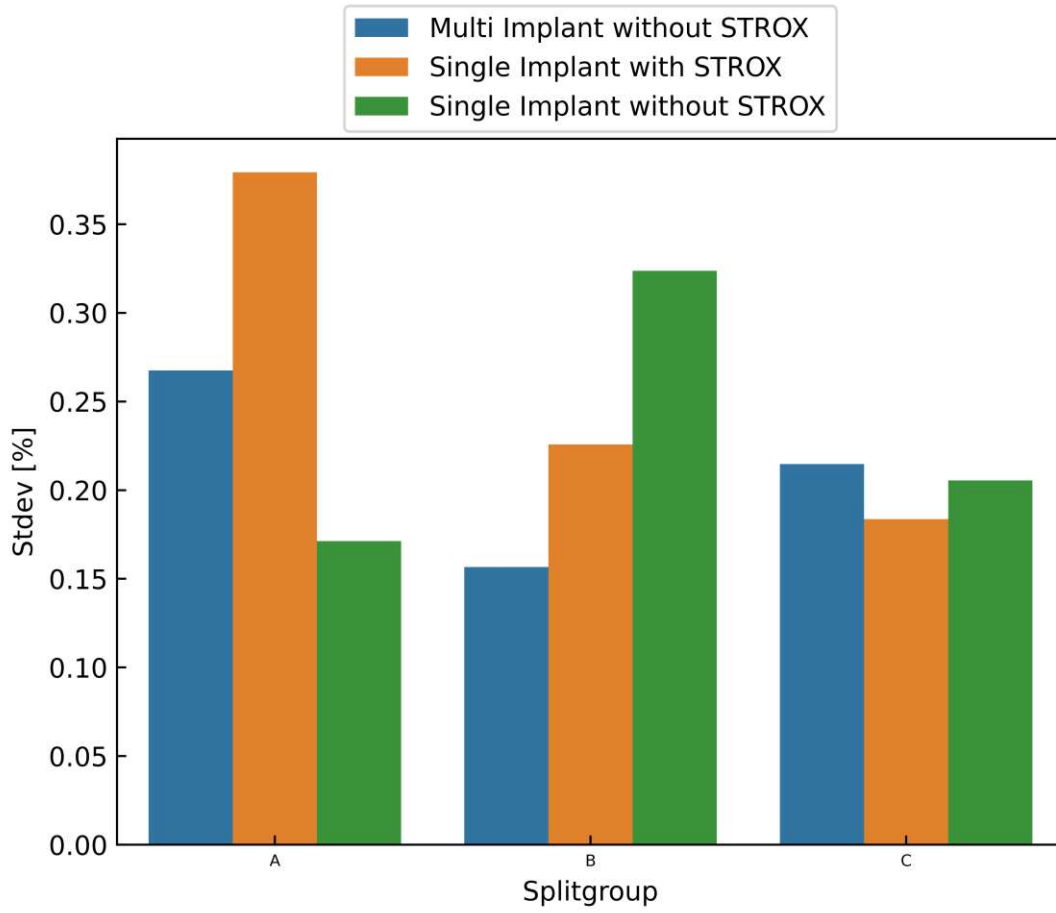
Figure 4.7: Run-to-Run standard deviations of the sheet resistance

Chapter 5

Test Structures for 4-point-probe Measurement

As a second way to improve the accuracy of the dose measurement, test structures for a four-point-probe measurement were designed. The basic layout for the structures was provided at the start of the thesis by Infineon Austria Technologies AG. A main part of the work focussed on adjusting the design and process flow to ensure sufficiently good contact to the layer to be measured and isolation between test structures, as well as between structures and the underlying substrate.

The idea to monitor implantation processes with structures is not a novel concept. McCarthy and Lukaszek [35] designed test structures to monitor shadowing, channeling and dose uniformity for p- and n-type implants for ULSI fabrication. They used contact implants above $10^{15}\,\mathrm{cm}^{-2}$ to contact the active implant. Per their design, the measurement of p-type and n-type Implants was not achieved in a single structure, but by switching all dopant types during the processing. A similar approach to different implant species was taken for the structures developed during this thesis.
Using test structures with a defined geometry allows the monitoring of a wide dose and energy range, as there is no limitation to place the implant close to the wafer surface.

5.1 Basic Design and Functionality

The test structures, comprised of 11 different chip variations, were designed to allow a four-point measurement of the implanted layer, without measuring the underlying substrate or the layer within the neighbouring chips. Figure 5.2 shows chip variation 1 representatively for variations 1-8 and 11. Variation 9 is similar to 10. The striped area and the area showing the number 1 are not part of the active structure. These areas are used to make optical differentiating between chips easier. As seen in the figure, the contact pads, where the needles for the resistance measurement are placed, are connected to the active area with strips of the same material as the pads. They cross the oxide filled isolation trenches at several points. For the chip variations 9 and 10 the strips are directly connected on the surface. For all other variations the strips are separated and electrically connected with the implanted layer.
The chips are comprised of 3 lithography layers. Layer 1 is used for isolation. An epitaxial
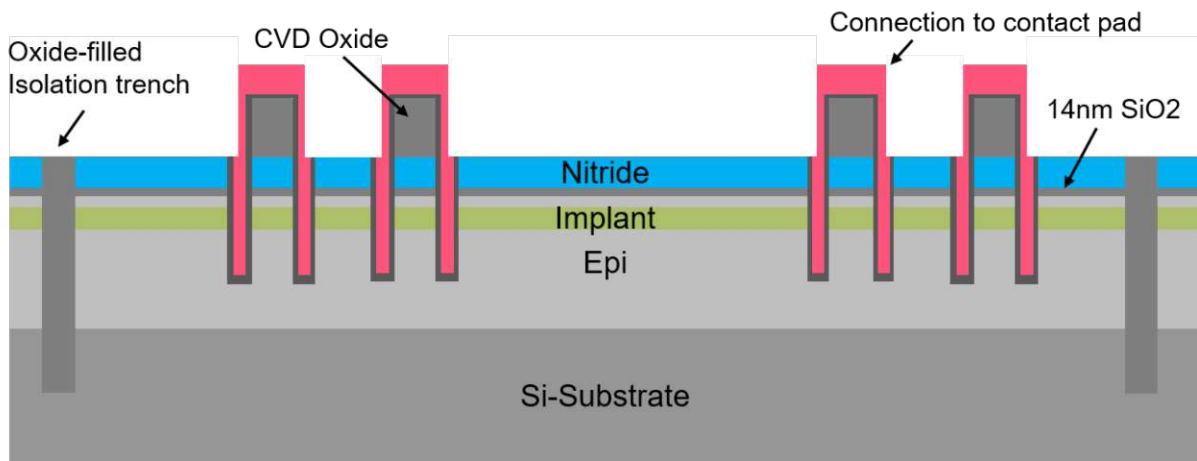
Figure 5.1: Schematic cross section of the active area

silicon layer (EPI) is grown on the substrate, followed by the deposition of a thin SiO2 layer and a SiN layer. During the subsequent high temperature steps dopants diffuse from the substrate into the EPI layer. The EPI changes its type from undoped to n- or p-type, depending on the substrate type. An oxide hard mask is deposited and structured with lithography layer 1. Trenches are etched through the nitride, oxide and EPI, ending in the substrate. These trenches are then filled with thermal oxide and used to isolate the chips from each other as well as isolating parts within the chips.

Another oxide layer is deposited, structured with lithography layer 2 and used as a hard mask for the etch of the contact trenches. The contact trenches go down to the middle of the EPI layer. This ensures, that the trench is deep enough to contact the implant later on, but the trench is still shallow enough, that the isolation trenches are deeper. To create a good contact, the contact trenches are implanted. The implant conditions can be taken from table 5.4.

After the implant the trenches are filled with highly n-doped poly-Si. The poly-Si serves as a contact between the implant to be measured and the contact needles of the measurement tool. It is structured with the third lithography layer and a plasma etch process.

The finished structures are then cleaned, implanted, annealed and measured. Figure 5.1 shows a schematic cross section through the active area of a chip. The position of the implanted layer, which is measured is marked in green.

All chip variations are $2\,\text{mm} \times 3\,\text{mm}$ big and have identical contact pads. The main difference is the position of the contact trenches and the resulting difference in the area to be measured. As can be seen in figure 5.2 the active area marked with the number 3 is $100\,\mu\text{m}$ wide and $250\,\mu\text{m}$ long.

In chip variation 2 the width is equal to that of chip variation 1, but the length is doubled. With the use of formula 3.5 it immediately follows, that the measured resistance for chip 2 is double that of chip 1, assuming, that everything else apart from the length stays the same. Doubling the width leads to the opposite effect on the measured resistance, meaning that the resistance should stay constant in case of doubled length and width. The length and width of the active areas for all chip variations can be taken from table 5.1. With the exception of chip variations 9 and 10, all measured resistances can be compared to the resistance of chip variation 1. Due to the direct connection between the contact
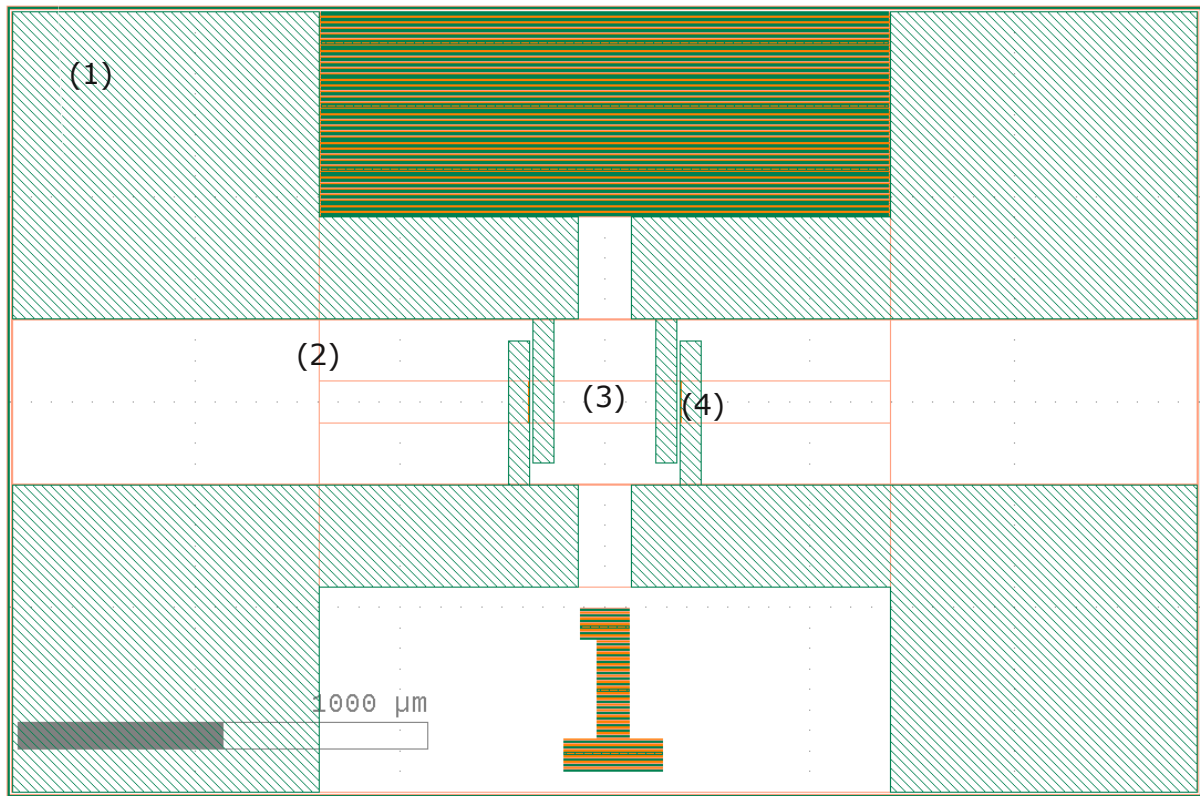
Figure 5.2: Top view of chip variation 1. (1) Contact pad, (2)
Isolation-trench, (3) Active area, (4) Contact trench

pads for chip variations 9 and 10, these variations allow the measurement of the resistance of the contact material.

The variety of implant area sizes allows the measurement of a range of implant doses. High implant doses resulting in low resistances can be measured more accurately with high ohmic structures, while low doses can be measured with low ohmic structures. This would allow the monitoring of doses across the whole range used for productive implants, as opposed to only measuring doses in the optimal measurement range for sheet resistances.

5.2 Dose variation

The structures were tested with implant doses in the range of $1 \times 10^{13}\,\mathrm{cm}^{-2}$ to $1 \times 10^{15}\,\mathrm{cm}^{-2}$. As the implant species boron and phosphorus were selected. Energies were chosen based on the thickness of the nitride layer over the active area to ensure that the ions were fully incorporated in the silicon and not in the nitride.

Ion implantation took place through a nitride layer of either $140\,\mathrm{nm}$ or $60\,\mathrm{nm}$ thickness. Implantation after complete removal of the nitride and padoxide layers were tested as well. In this case a tilt of $7°$ and twist of $23°$ was used. All other implantations took place without tilt.
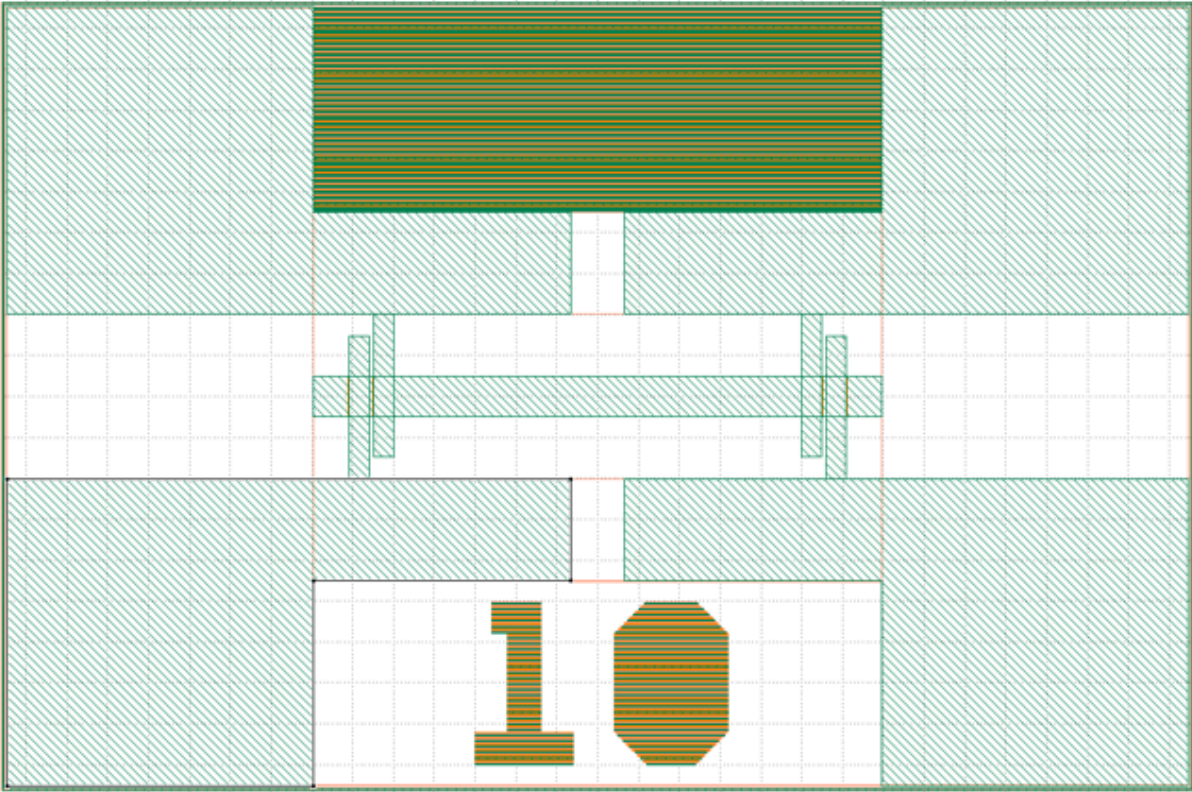
Figure 5.3: Top view of chip variation 10, a shorted structure for the measurement of the contact resistance

Table 5.1: Length and width of the active area for each chip variation with the expected resistance based on the resistance of chip variation 1, R_C denotes the contact resistance

Chip	Length [µm]	Width [µm]	R Verhaeltnis
1	250	100	R
2	500	100	2R
3	1000	100	4R
4	500	200	R
5	1000	200	2R
6	130	40	1.3R
7	260	80	1.3R
8	520	160	1.3R
9	130	40	R_C
10	1000	100	R_C
11	4740	40	47.4R

5.2.1 Phosphorous Implants after Nitride and Oxide Etch

The nitride layer above the active area was completely removed with Hot Phosphoric Acid on 2 wafers with Poly-Si contacts. Wafer 1 was implanted with phosphorus $1.0 \times 10^{15} \, \text{cm}^{-2}$ at 285 keV, without tilt or twist angles. Wafer 2 saw an additional HF process to remove the thin Pad-oxide beneath the nitride layer. To avoid channeling, wafer 2 was implanted with the same energy and dose as wafer 1, but with a tilt of 7° and a twist of 23°.

Figure 5.4 shows ΔR [%] over the wafers. The values corresponding to measurement site 0 had to be removed due to a measurement failure on that site. Wafer 1 shows a "sundown" like pattern, which might be due to contamination through the Hot Phosphoric Acid, since wafer 2 does not show this pattern.

The mean sheet resistance values after the geometry correction outlined in section 5.3.2 are $64.695 \, \Omega/\square$ for wafer 1 and $65.757 \, \Omega/\square$ for wafer 2. These values are in good agreement with the theoretical value calculated with eq. (3.7a).

(a) Nitride etch (b) Nitride and Oxide etch
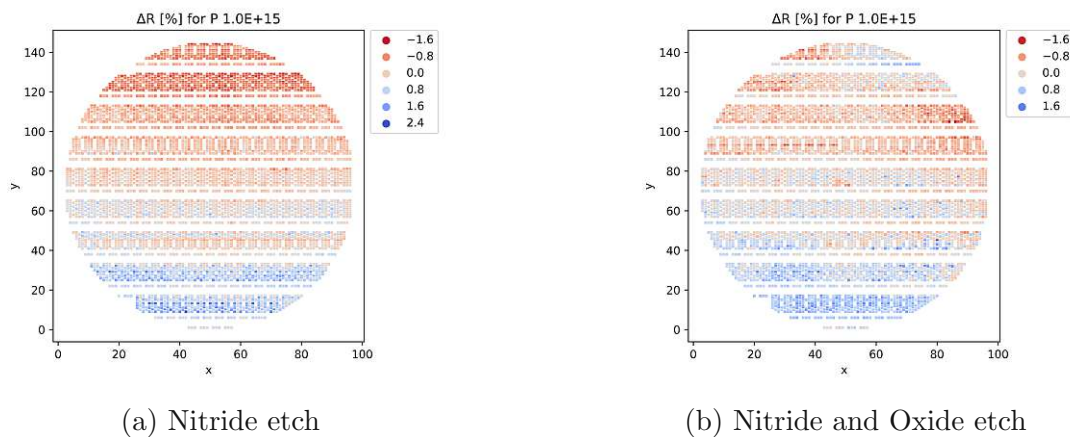
Figure 5.4: Difference in ΔR [%] for Removal of Nitride and Removal of Nitride and Pad-oxide.

5.2.2 Phosphorous Implants through 60nm Nitride

5 Wafers with poly-Si contacts were subjected to an etching process. The 140 nm thick nitride layer above the active area was thinned to 60 nm. The wafers were implanted with phosphorous in the doses $1.0 \times 10^{13} \, \text{cm}^{-2}$, $5.0 \times 10^{13} \, \text{cm}^{-2}$, $2.0 \times 10^{14} \, \text{cm}^{-2}$ and $5.0 \times 10^{14} \, \text{cm}^{-2}$ at 350 keV without a tilt angle. A second wafer with $2.0 \times 10^{14} \, \text{cm}^{-2}$ was implanted with a twist angle of 90° to verify if the signature seen on the wafer is caused by the implanter or noise.

Figure 5.5 shows the sheet resistance of the different wafers after deduction of the contact resistance. Figure 5.5 shows the sheet resistance calculated from the measured resistances and the ideal chip dimensions given in table 5.1 after deduction of the contact resistance. Chip variations 9 and 10 were excluded, since they are used to measure the resistance of the contact material and are therefore independent of the implanted dose. The median values for the depicted chipvariations are within $20 \, \Omega/\square$ of the theoretical values calculated with eq. (3.7a). For variations 1, 2 and 3 the medians are very close for all implant doses. This is also the case for variations 4 and 5, which have the same length as 1 and 2, but twice the width. They show a downward offset. It is notable, that for these 5 variations the standard deviation becomes smaller with increasing length of the active area. For
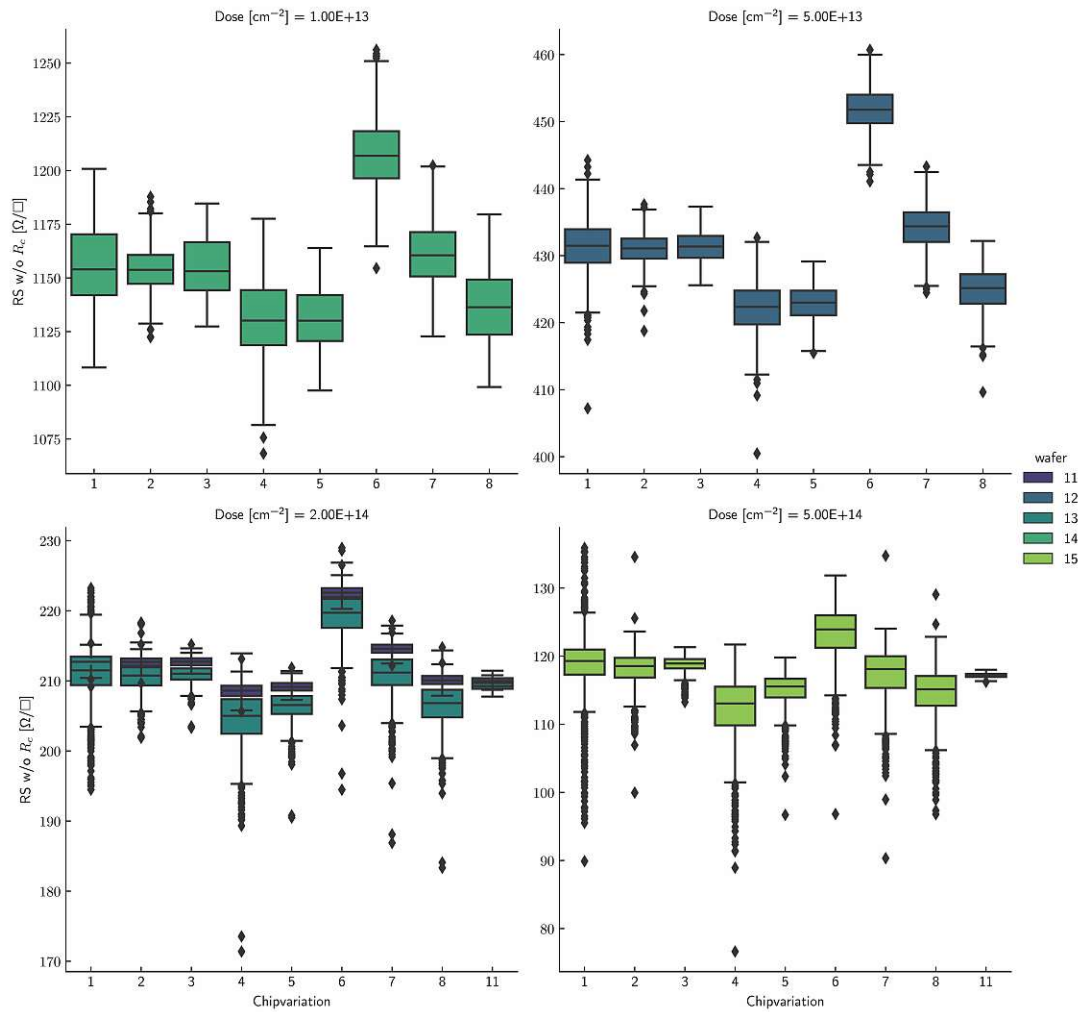
Figure 5.5: RS without contact resistance for phosphorous implants.

variations 6, 7 and 8 the sheet resistance decreased with an increase in area, as for chip variation 7 the active area is 4 times as large as that of variation 6 and for variation 8 it is 16 times as large. The standard deviation showed no change with the area size. For the doses were the high-ohmic variation 11 was measurable, the median sheet resistance of this structure was close to that of variations 1, 2 and 3. Variation 11 resulted in the smallest standard deviation. The sheet resistances for wafers 11 and 13 are in good agreement with each other, but for wafer 11 the standard deviations are smaller for all chip variations and a slight offset is observed.

The standard deviations for the sheet resistance correspond to standard deviations in the implanted dose. The values can be taken from table 5.2. It is notable, that the lowest standard deviations were observed on wafer 11, where the values were consistently $\leq 0.6\,\%$. Chipvariation 1 resulted in the highest deviation on all 5 wafers, variations 3 and 11 resulted in relatively low deviations. Fitting of the sheet resistance values with 4.2 resulted in the fit parameters $a = -0.561$ and $b = 23.811$.

Table 5.2: Standard deviations given in percent of the implanted
dose for each wafer and chipvariation

Chipvaritaion	1.0×10^{13} cm^{-2}	5.0×10^{13} cm^{-2}	2.0×10^{14} cm^{-2} +90° twist	2.0×10^{14} cm^{-2}	5.0×10^{14} cm^{-2}
1	1.05	1.41	0.60	3.87	7.84
2	0.71	0.59	0.51	0.91	1.65
3	0.70	0.53	0.50	0.50	0.57
4	0.81	0.77	0.66	1.27	2.31
5	0.71	0.52	0.52	0.59	0.93
6	0.89	0.64	0.53	1.00	1.78
7	0.82	0.58	0.51	0.74	1.35
8	0.77	0.61	0.56	0.97	1.60
11	-	-	0.49	0.54	0.48

5.2.3 Boron Implants through 60nm Nitride

Analogue to section 5.2.2 5 Wafers with ALD Ti/TiN and poly-Si contacts were subjected
to an etching process. The 140 nm thick nitride layer above the active area was thinned to
60 nm. The wafers were implanted with boron in the doses 1.0×10^{13} cm^{-2}, 5.0×10^{13} cm^{-2},
2.0×10^{14} cm^{-2} and 5.0×10^{14} cm^{-2} at 150 keV without a tilt angle. A second wafer with
2.0×10^{14} cm^{-2} was implanted with a twist angle of 90° to verify if the signature seen on
the wafer is caused by the implanter or noise.

For the wafers with doses in the 10^{13} cm^{-2} range chip variation 11 was to high ohmic to be
measured with the used program. This variation is therefore not included in the results
for these wafers. Chipvariations 9 and 10 were excluded.

As seen in fig. 5.6 the variation of the sheet resistance is smaller for chipvariations of
greater length. This is evident for the variations 1,2 and 3, for which the length doubles,
while the width stays the same, especially for wafers that were implanted with higher
doses. The high ohmic chipvariation 11 shows the smallest variation. Contrary to the
expectation, chipvariations 6, 7 and 8 did not show the same same sheet resistances and
variations. They also showed lower sheet resistances and variations for greater lengths.

The mean sheet resistance values for the wafers implanted with doses in the 10^{14} cm^{-2}
range were in good agreement with those calculated with eq. (3.7b). For lower doses the
theoretical values were far from the measured ones, as the lower limits of the validity
range was reached.

All wafers showed a radial pattern of ΔR [%]. An influence of the twist angel was therefore
not seen. A fit of the sheet resistances plotted over the implanted doses was calculated.
The fit parameters were $a = -0.577$ and $b = 24.816$.

Table 5.3 shows the standard deviations of the implanted dose in percent for all chip-
variations. They were calculated from the measured resistances after deduction of a fit
of the radial pattern. For wafer 7 implanted with 2.0×10^{14} cm^{-3} boron, the pattern
was more elliptical, than a circular radial pattern. It is notable, that for the two wafers
implanted with 2.0×10^{14} cm^{-3} one showed relatively high deviations for all but three chip
variations and for both variation 11 resulted in a deviation above 1.1 %. For the wafer
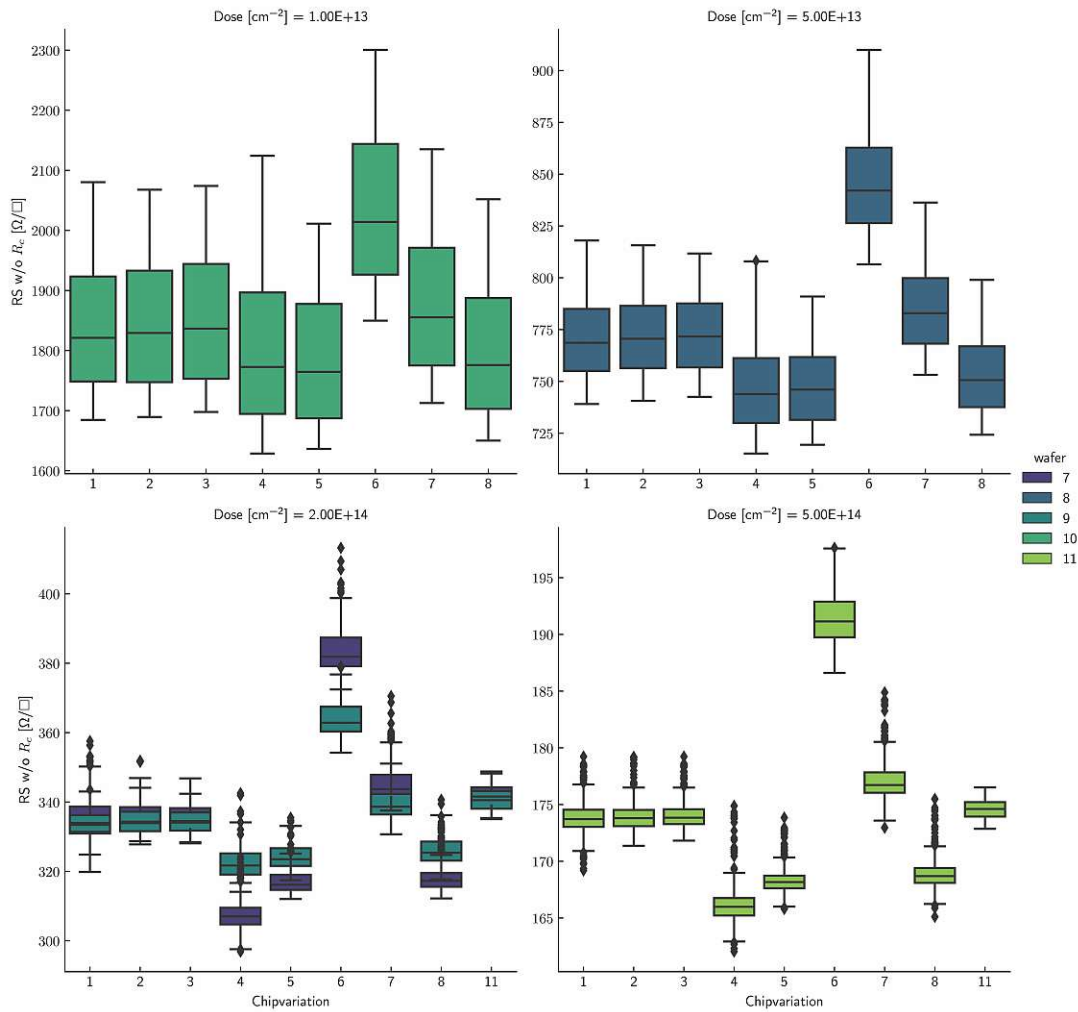
Figure 5.6: RS without contact resistance for boron implants through
60 nm nitride.

Table 5.3: Standard deviations given in percent of the implanted
dose for each wafer and chipvariation

Chipvariation	1.0×10^{13} cm^{-2}	5.0×10^{13} cm^{-2}	2.0×10^{14} cm^{-2}	2.0×10^{14} cm^{-2}	5.0×10^{14} cm^{-2}
				$+90°$	
1	0.83	0.52	1.61	0.50	0.76
2	0.71	0.44	0.88	0.28	0.33
3	0.72	0.40	0.50	0.25	0.24
4	0.79	0.45	1.28	0.34	0.41
5	0.75	0.41	0.70	0.22	0.28
6	0.86	0.63	1.31	0.48	0.57
7	0.81	0.47	1.32	0.35	0.44
8	0.78	0.44	1.14	0.31	0.35
11	-	-	1.55	1.40	0.18

implanted with $5.0 \times 10^{14}\,\mathrm{cm}^{-3}$ the high-ohmic structure 11 showed the lowest standard deviation.

5.3 Disturbing Influences

During the determination of the final process flow for the measurement structures, a number of issues have emerged. They resulted either in unmeasurable structures or in effects that added strong resistance variations and overshadowed the effects of the implanter. These issues must be addressed to make the structures useful for implanter monitoring.

5.3.1 EPI

While no dopants are actively directed into the process chamber during the growth of the EPI layer, a background doping due to residual dopants from preceding processes can not be ruled out. For a lot that receives this process, the effect of the background doping is strongest for the first wafer and decreases with each wafer in the lot. Depending on the preceding dopant type and dose, the effect on the measurement varies. Since the EPI takes on the dopant concentration of the substrate material, a variation in the EPI layer can be counted as a variation in the substrate doping. Measurements showed the background doping to be below $5 \times 10^{13}\,\mathrm{cm}^{-3}$. The n-doped material used for the measurement of p-type implants had dopant in the range of $3 \times 10^{13}\,\mathrm{cm}^{-3}$ to $1.1 \times 10^{14}\,\mathrm{cm}^{-3}$.

5.3.2 Furnace

High temperature steps influence the sheet resistance with the difference in diffusion and activation of dopant atoms. Concerning the operations involved with the whole process, a division into furnace steps before and after the ion implantation is possible.

The first group includes the filling of the isolation-trenches with thermal oxide at $1000\,°\mathrm{C}$ and the annealing of the poly-Si contacts. After the implantation of the active dopants, the wafers were annealed with an RTP step at $1040\,°\mathrm{C}$ to activate the active and contact implants. For the high temperature steps, two factors need to be taken into account. The implants must be fully activated after the RTP step, and a diffusion of dopants from the highly n-doped poly-Si into the active area must be prevented or included in the final analysis of the measurement.

A geometry correction was performed to account for possible diffusion effects. It was calculated separately for each wafer. The chipvariations 9, 10 and 11 were excluded. First the Median of the measured values per chipvariation was multiplied with the ideal width of the chipvariation and plotted over the ideal length. Then a straight line was fitted to the data points, resulting in eq. (5.1).

$$R \cdot W = k \cdot L + d \tag{5.1}$$

Setting eq. (5.1) to 0 and solving for L returns the offset between the ideal length and the actual length.

The substitution of L with $L + dL$ is then used for the correction of the width. Here the corrected length is divided by the Median of the measured values, before the linear fit is

used. The offset of the width dW is calculated similar to dL. The corrected length and width can then be used to calculate the sheet resistance from the median values.

5.3.3 Variation of layer thickness over the wafer

The variation of the thickness of a layer over one wafer must be considered, if the ion implantation takes place through this layer. According to the process described in section 5.1, the ion implantation would take place through a 140 nm thick SiN layer and 14 nm SiO2. If the thickness of these layers is uniform across the wafer, the profile of the implanted ions is also uniform. In the event of thickness variations, such as a radial pattern where the layer is thinner in the wafer middle than on the edge, the pattern is also reflected in resistance measurements. Changes in the resistance value can result from dopants, that are stuck in the SiN or SiO2 layer and do not contribute to the conduction. Another possibility is the shift of the implant profile to different depth.
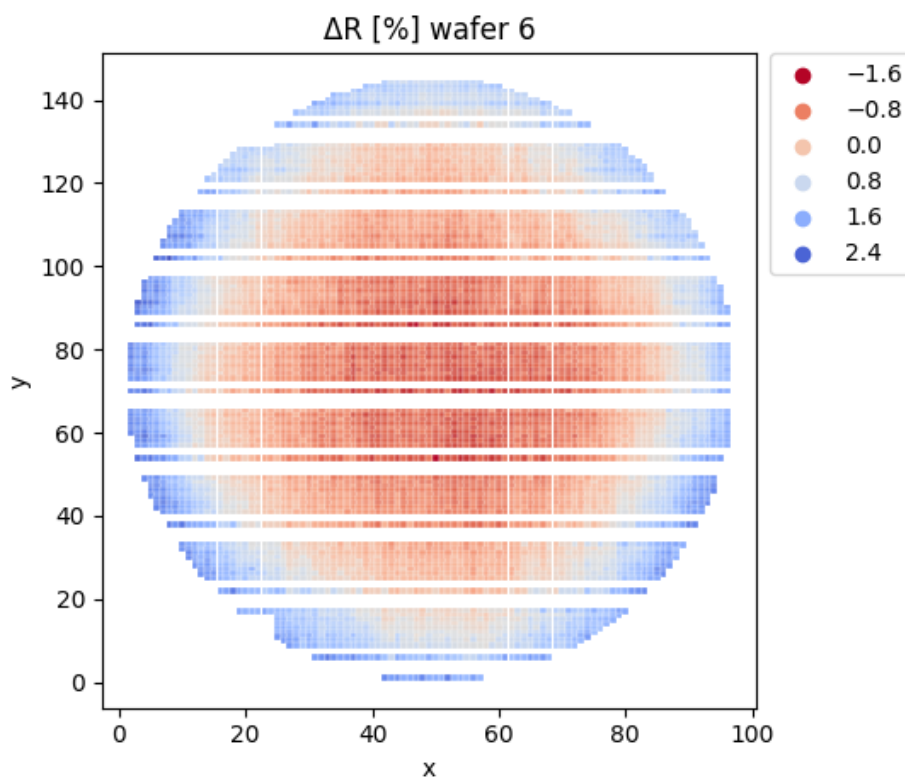
Figure 5.7: Wafermap of a wafer implanted with 2×10^{14} cm^{-2} phosphorus at 350 keV. The color indicates the difference of the measured resistance to the median of each chip type in percent

Figure 5.7 shows the pattern in the measured resistances for a wafer, that was implanted with 2×10^{14} cm^{-2} phosphorus at 350 keV. Since the chipvariations result in different absolut resistance values, the values were normed on the median of their respective chipvariation. To make the chipvariations comparable, the figure shows ΔR [%], the difference to this median in percent, as the hue over the wafer. The color pattern from red to blue shows that the resistance increases with the radius.

Table 5.4: Implant parameters for the contact implant conditions
for p- and n-type implants

Parameter	1. Implant	2. Implant	1. Implant	2. Implant
Dose [cm^{-2}]	4.0×10^{14}	4.0×10^{16}	3.0×10^{15}	3.0×10^{14}
Energy [keV]	80	15	20	20
Species	boron	BF2	As	P

5.3.4 Contact implants and materials

A major difficulty with the structures was contacting the implanted layers. To ensure a good contact, contact implants with high doses and low energies were used. In table 5.4 the conditions for the contact ion implants are listed. The dopant profile was created in two steps. All implants were performed with a tilt angle of 30° in quad-mode. In this mode a quarter of the dose is implanted, then the wafer is twisted by 90°, again implanted with a quarter of the dose and so on. The quad-mode ensures, that the contact implant is embedded in all 4 side-walls of the contact trench. The combination with the high tilt angle prevents shadowing effects on the trench bottom, while guaranteeing full coverage of the side walls. First a high dose was implanted near the surface for a good contact between the contact material and the implanted layer. Then a secondary implant was added to enlarge the contact implant zone.

BF2 was chosen for the near surface implant for p-type implants, because it requires higher implant energies to reach the same depth as a boron implant due to the difference in mass. The energy is divided among the three atoms according to the law of mass action. [36] A BF2 implant with 15 keV creates therefore a dopant depth profile that is similar to that of a boron implantation with 3.32 keV. The change in implant species was necessary, as 3.32 keV were too low for the used implantation tools.

The process flow described above for the creation of a structure to allow a four-point measurement of a phosphorus implant works perfectly fine, due to both implant and poly-Si contacts being n-doped. While it would be preferable to switch the dopant type of the poly-Si to p-type for the measurement of boron implants, it was not possible for the experiments done during the course of this thesis, as the process was not yet available for 12" wafers. This resulted in a pn-junction between the p-type ion implant and the n-type poly-Si used as a contact. During the measurement half of the created pn-junctions are operated in reverse direction, resulting in no measurable output, due to the increase in the space charge region.

The following possible ways to contact a boron implant with the given process requirements were explored.

TiSi2 and Poly-Si

To create a contact to the implanted layer, a Titandisilicid (TiSi2) liner was added to the contact trenches, before filling them with poly-Si. The TiSi2 was meant to create a semiconductor-metal contact. For this purpose a Titan-Liner was deposited via sputtering and annealed with a RTP step at 740 °C to form TiSi2 where the Ti was in contact with underlying Si. The part of the Ti that remained was removed with an etching process,

leaving TiSi2 only in the contact trenches. The trenches were filled with n-doped poly-Si and annealed at 975 °C.

After the poly-Si deposition, the wafers were further processed with the procedure outlined in section 5.1. The wafers were implanted, annealed and cleaned under the same conditions as the wafers with basic poly-Si contacts. The subsequent resistance measurement showed values in accordance with those above for phosphorus implants. Boron implants were not measurable with this contact variation.
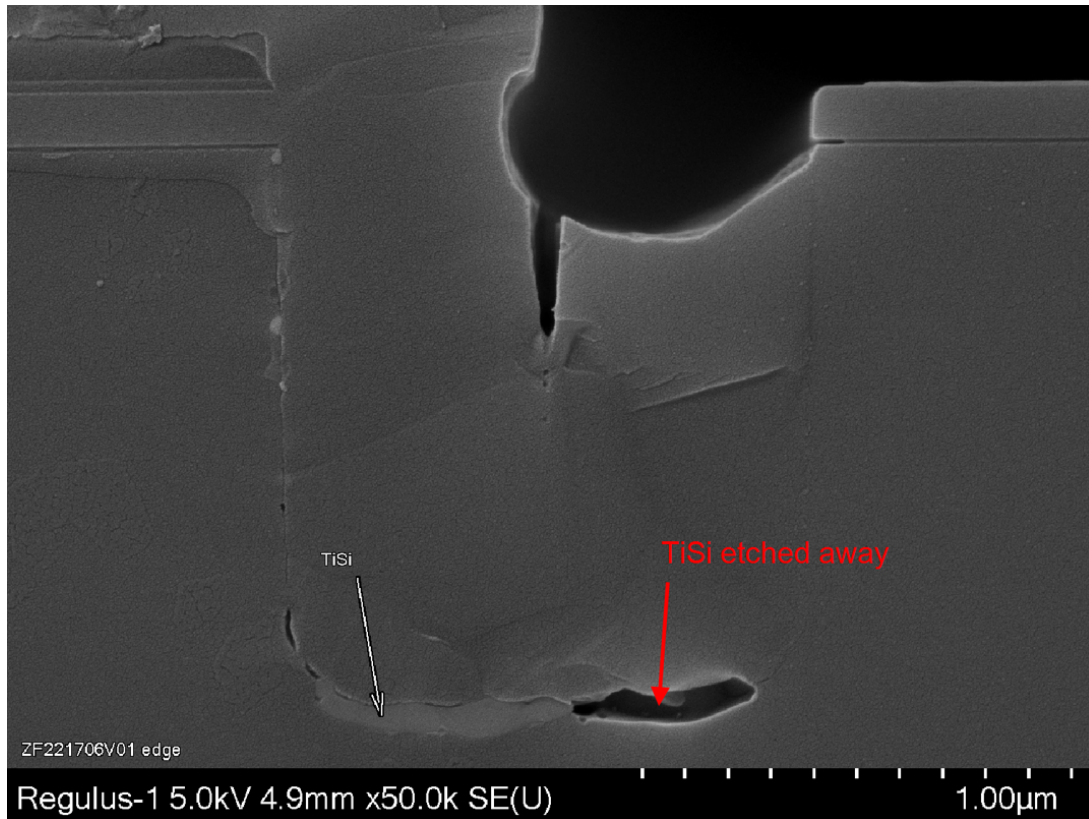
Figure 5.8: SEM image of a chip cross-section where a TiSi2 liner was used

Figure 5.8 shows a contact trench that is representative for the TiSi2 + poly-Si contact variation. As seen in figure fig. 5.8 most of the TiSi2 agglomerated at the bottom of the contact trench, with only minimal TiSi2 remaining on the side walls. It is not clear if the voids were a result of the agglomeration process or if chunks of the TiSi2 broke off during the preparation process for the SEM measurement.

Ti/TiN and Tungsten

The poly-Si contact was substituted with a Ti/TiN Liner and a Tungsten Plugfill process to create a metal semiconductor junction. A 40 nm thin Ti/TiN-Liner was deposited via sputtering and annealed to form TiSi2, before the trenches were filled with Tungsten through Modified Chemical Vapor Deposition (MCVD). The high wafer bow resulting from the Tungsten deposition was reduced through a plasma etching process, which thinned the Tungsten layer on the surface from 800 nm to 330 nm. The subsequent structuring of the Tungsten layer, as well as the cleaning, oxide etch and implant steps had to

be adjusted to be possible without contaminating the necessary tools.

Removing the nitride layer above the active area with a wet chemical etching was not possible due to the open tungsten. Figure 5.9a shows a SEM image of a FIB-Cut taken on a wafer after structuring of the tungsten contacts and removal of the overlying oxide. The hollowed out area marked with the red arrow shows an underetch of the silicon. The energy for the ion implantation was increased accordingly to $285\,\text{keV}$ for boron implants with $1.0 \times 10^{14}\,\text{cm}^{-2}$ and $1.0 \times 10^{15}\,\text{cm}^{-2}$ through the nitride layer. A tilt angle of $7\,\text{degree}$ and a twist of $23°$ were used.

The wafer surface was covered with $250\,\text{nm}$ SiO2 before the annealing took place to mitigate the contamination risk. The SiO2 layer was removed with HF before the measurement.

As seen in fig. 5.9c and fig. 5.9d, the measured resistances are significantly higher for x values in the range of 25 to 70 and partially missing for some chips. Excluding the values in this range and recalculating ΔR [%] reduces the range to $-10\,\%$ to $15\,\%$, which is still significantly higher than the target deviation. Using the ideal chip measurements for the conversion from Ω to $\Omega/\square$ leads to a mean sheet resistances of $563.687\,\Omega/\square$ and $141.820\,\Omega/\square$ for boron implant doses of $1.0 \times 10^{14}\,\text{cm}^{-2}$ and $1.0 \times 10^{15}\,\text{cm}^{-2}$ respectively. The standard deviations for both wafers were above $20\,\Omega/\square$. The missing values are due to missing or damaged connections between the contact trenches and pads. Contact strips were partially bend up, broken at the edges or entirely missing. Bend up of the contact strips started at the ends that were not connected to the pads as seen in fig. 5.9b. It is plausible, that a combination of mechanical stress and underetching of the strips during the removal of the final oxide layer lead to the damage.

ALD Ti/TiN and Poly-Si

For the fourth contact variation that was tested, a Ti-Liner was deposited with Atomic Layer Deposition (ALD), followed by a TiN-Liner. ALD allows a better coverage of the trench side walls than deposition with sputtering. After the Liner deposition, an annealing step took place, before the poly-Si was deposited.

Figure 5.10a shows a schematic version of a contact trench cross section. The TiSi2- and TiN-Liner cover the whole trench. This is also evident in fig. 5.10b, where the Liner is the thin white line marked with the red arrow. The TiSi2-Liner creates the contact to the implanted layer and the TiN-Liner acts as a diffusion barrier for the dopants of the n-type poly-Si.

The monitoring of boron implants is possible with this contact variation.

5.3.5 Needle Placement

The resistance measurement for the structured wafers was performed with an EAGLE basischip measurement system, with a needle probe card which fit the wafer layout. 4 Chips were measured at a time, corresponding to the sites 0, 1, 2, 3. For wafers where the influences outlined above were eliminated, a pattern emerged in the wafermap plots of ΔR [%]. A comparison between ΔR [%] and the measurements sites indicates, that one of the measurement sites returns higher values than the other 3 sites. This is shown in fig. 5.11a for a wafer segment. Figure 5.11b shows the corresponding measurement sites that were used to measure the wafer segment. Measurement site 3 in fig. 5.11b corresponds to the
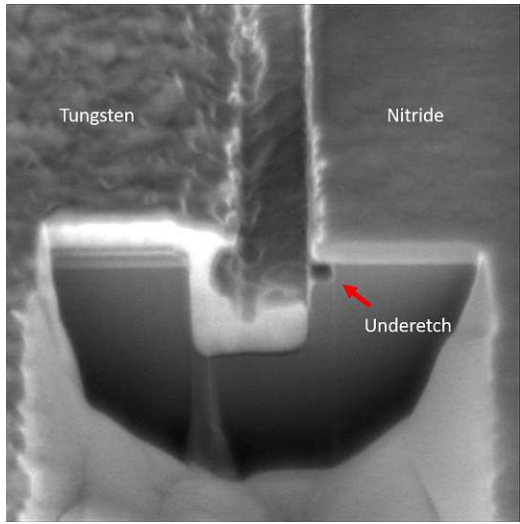
(a) SEM image of contact trench after FIB-Cut
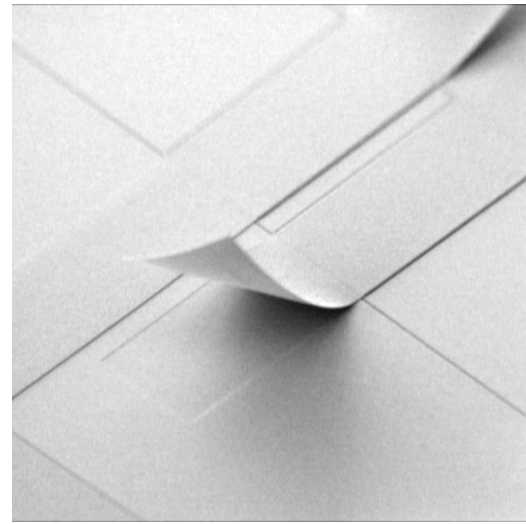
(b) SEM image contact strips
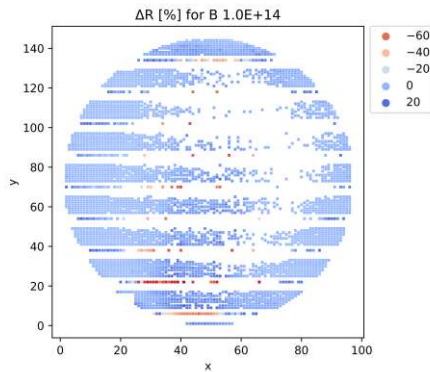
(c) ΔR [%] boron $1.0 \times 10^{14}\,\mathrm{cm}^{-2}$
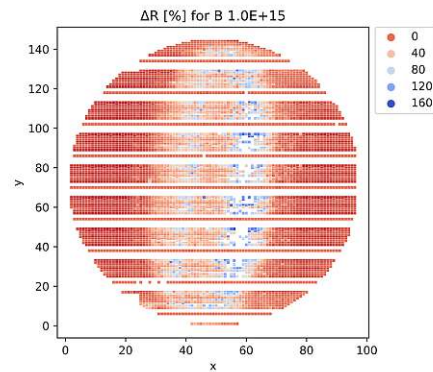
(d) ΔR [%] boron $1.0 \times 10^{15}\,\mathrm{cm}^{-2}$

Figure 5.9: SEM images of contact trench cross section for variation Ti/TiN and Tungsten after oxide etch and bend up of contact strips. ΔR [%] after boron implantation

higher values of ΔR [%], which are marked with blue hues in fig. 5.11a. This was the case for most measured wafers, where the pattern was seen and not obstructed by other influences. For a handful of wafers the outlier was site 0. The reason was traced to a higher leakage current on the outlying sites during the measurement. To counter this effect, the calculation of ΔR [%] was adjusted. Further ΔR [%] values were calculated as the deviation from the median after grouping the data by the chipvariation and the measurement site.

Outliers were classified through a standard score outside of ± 2 and discarded.

(a) Schematic of contact trench

(b) FIB-Cut and SEM image
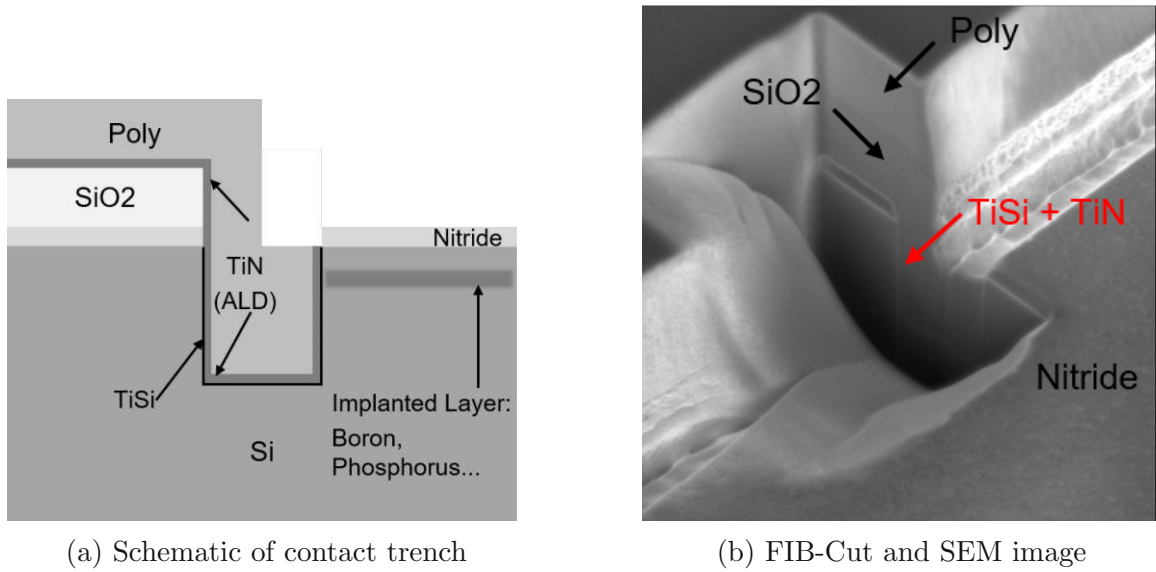
Figure 5.10: Schematic and SEM image of contact trench cross section
for variation ALD Ti/TiN and Poly-Si
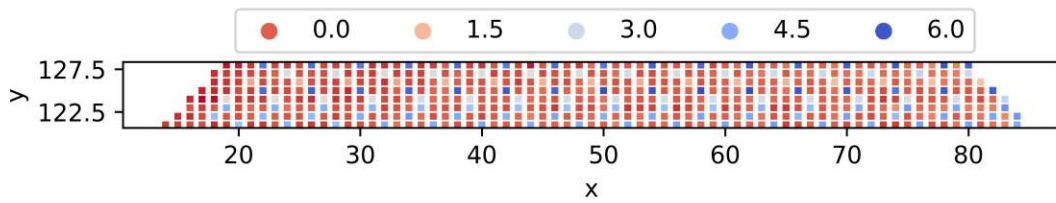
(a) Wafermap section with ΔR [%] as hue
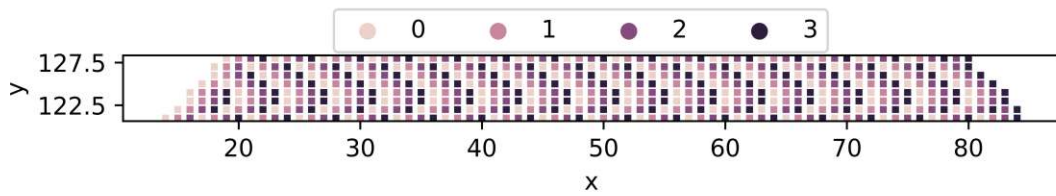
(b) Wafermap section with the measurement sites as hue

Figure 5.11: Comparison of ΔR [%] to the measurement sites for a
wafer section

48

Chapter 6

Wafer ageing

During remeasurements of implanted unstructured wafers, a change in sheet resistance was seen. To exclude an influence from the measurement tool itself, the wafers were remeasured on 3 different 4-point-probe tools of the same variety on site in Villach, shipped to the Infineon site in Dresden and measured again with all available tools. All tools showed the change.

Data from an 8" wafer that was repeatedly measured between 2018 and 2022 showed, that the effect was not limited to 12" wafers, therefore excluding an influence of process tools used for implantation, cleaning and annealing, since the wafer diameter demanded different tools for these processes. The 8" wafer started with a mean value of $500\,\Omega/\square$, measured within $6\,\mathrm{h}$ of implantation and annealing. It showed an increase of approximately $10\,\Omega/\square$ within the first 120 days and another $10\,\Omega/\square$ until 2022. Over a period of 4 years, the effect seems to reach a saturation.

If the intention of multiple measurements is to use the wafer as a reference to monitor the measurement tool, then the sheet resistance of the wafer must be constant. To ensure that, it is necessary to determine what triggers the change.

6.1 Time dependent Drift of Sheet Resistance

Remeasurements of unstructured implanted and annealed wafers showed an increase in sheet resistance with time. This effect was observed on every unstructured wafer, that was measured more than once over time. Figure 6.1 shows the change in the measured sheet resistance for a number of wafer, that were implanted with boron or phosphorus with a dose of $1.5 \times 10^{14}\,\mathrm{cm}^{-2}$ with $45\,\mathrm{keV}$ and $115\,\mathrm{keV}$ respectively. The process flow followed section 3.5.

All wafers were processed at different times over the course of a month, the x-axis of fig. 6.1 depicts the difference between the measurement dates and their respective annealing dates. Wafers implanted with the same species show the same qualitative behaviour, but the absolute measured values differ.

An influence of the process equipment could be excluded, due to results from the Metrology Department, which showed that the effect is also seen in 8" wafers, which are processed with different equipment, than the 12" wafers used for this thesis. Furthermore, the influ-

ence of the measurement equipment itself could also be excluded, due to remeasurements with two different tools of the same type on site, as well as with two tools at the Dresden site, that showed the same result.

The wafers did not see further processes between the original measurement and the remeasurement apart from the transport to the store on site or to the site in Dresden.
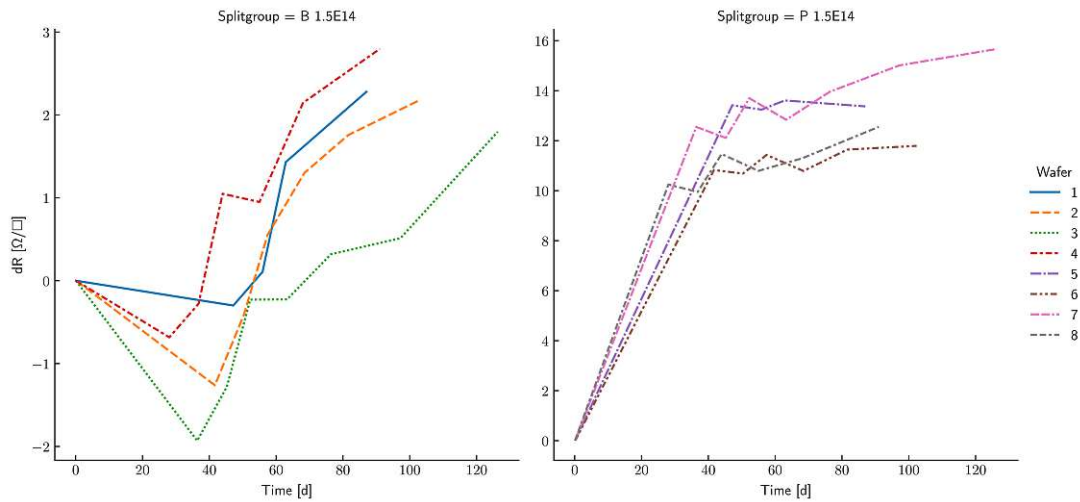
Figure 6.1: Sheet resistance change over time for wafers implanted with $1.5 \times 10^{14} \, \text{cm}^{-2}$ boron or phosphorus
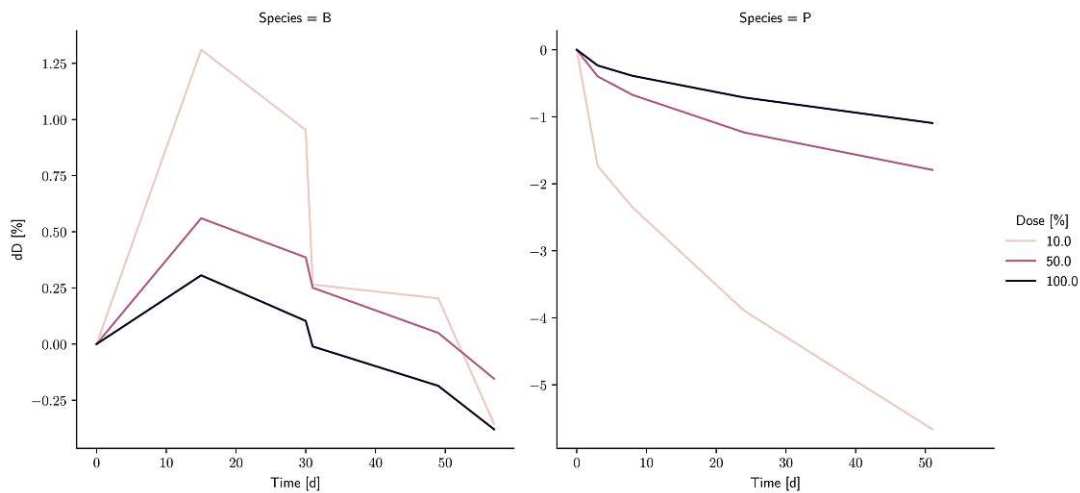
Figure 6.2: Dose loss in percent over time in days for boron and phosphorus implanted with $1.5 \times 10^{13} \, \text{cm}^{-2}$ (10 %), $7.5 \times 10^{13} \, \text{cm}^{-2}$ (50 %) and $1.5 \times 10^{14} \, \text{cm}^{-2}$ (100 %)

Figure 6.2 shows the qualitative difference in the behaviour of boron and phosphorus implants over time. The values on which the graph is based were calculated from the differences between the measured values over time through the use of the sensitivity values in table 4.4. Boron shows a slight increase in dose within the first 15 days after the initial measurement and decreases steadily after that. It is notable, that the median of the sheet resistance for the 10 % wafer (B10) corresponded to an increase in dose by $+1.311 \, \%$, while the wafer with 100 % (B100) only reached $+0.306 \, \%$. The 50 % wafer

(B50) showed an increase of $+0.560\,\%$, indicating, that the influence of the effect weakens with increasing implant dose in a non-linear manner.

Later measurements showed a dose loss of approximately $-0.38\,\%$ compared to the start value for both the B10 and B100.

Phosphorus on the other hand shows a drastic decrease of approximately $-1.734\,\%$ for P10 within the first 3 days. The naming convention mirrors that used for boron. After this its dose still decreases, but slower. P10 reached a dose loss of $-5.664\,\%$ after 51 days. For P50 the effect was significantly weaker with a loss of $-0.398\,\%$ and $-1.793\,\%$ at 3 and 51 days respectively. P100 reached $-0.234\,\%$ and $-1.093\,\%$

For both implant species the effect is stronger with lower implant doses, but qualitative similar within the dopant species.

6.2 Hydrogen-passivation and Bakeout

A possible theory for the change in sheet resistance is passivation due to hydrogen. Hydrogen in silicon is amphoteric, which means that it can exist in different charge states. This enables it to form bonds with a variety of defects, including vacancies, dangling silicon bonds and dopant atoms.[37], [38], [39] Due to the higher solubility at damaged surfaces, a high concentration of hydrogen can be absorbed, if it is included in the ambient gas. [40] The diffusion of hydrogen from the cleanroom air into the wafer and subsequent formation of various complexes, might account for the change in sheet resistance over time. Those formed complexes can be neutral, positively or negatively charged. At room temperature the formation of an electrically inert BH complex is possible. While other states, like the negatively charged BH2 exist and are favorable from an energetics point of view, the BH complex is the most stable, especially when the concentration of boron in the material is higher than the concentration of hydrogen. The formation of complexes is possible with molecular hydrogen and interstitial protons. In contrast, PH complexes are relatively unstable and dissociate at $100\,°C$. [41] As stated by De Guzman et al. "H effectively deactivates the electronic activity of boron upon formation of the BH and BH$_2$ defects. The BH$_2$defect is predicted to have a donor level at $E_C - E(0/+) = 90.24 eV$." [41]

To test the involvement of hydrogen in the reported sheet resistance change, two sets of experiments were done on wafers after storage and remeasurements. In the first set wafers showing the ageing effect were subjected to a series of heat processes in N2 atmosphere and remeasurements. During the second set, wafers were subjected to the same temperature steps in forming gas atmosphere. If hydrogen is involved, the sheet resistance should decrease at high temperature in N2 atmosphere due to the hydrogen defusing out of the sample, while for forming gas atmosphere, which has a high concentration of hydrogen, the opposite effect should be seen. In the range of $600\,°C$ to $700\,°C$, all possible hydrogen complexes should be dissolved and the doping of the wafer should revert to its original state. [42], [43] Figure 6.3 shows the results of the various 4-point probe measurements, starting with the original measurement in blue, followed by remeasured values after being stored under clean room conditions and after additional temperature steps. The temperature steps were set at $400\,°C$, $630\,°C$ and $800\,°C$ to assure the dissociation of possible Hydrogen complexes, while remaining below the temperature used for the initial annealing of the implant. They were carried out within $7\,h$ to prevent sheet resistance changes unrelated to the high temperatures.

A boron implanted n-type Si wafer showed a slight decrease in sheet resistance followed by an increase of $2.279\,\Omega/\square$ after storage for three months. After the series of temperature treatment cycles in N2 atmosphere the sheet resistance returned to the starting value. Storing the wafer for additional 2 months resulted in a reduction of the sheet resistance. Subjecting the wafer to an oven step at $400\,°C$ for 1 h in forming gas atmosphere resulted in a correction towards the starting value. Additional temperature steps with durations of 60 s reduced the values further, with the exception of the $1050\,°C$ step. This process resulted in an increase towards the starting values.

A phosphorus implanted wafer subjected to the same processes showed a rise of $13.37\,\Omega/\square$ during storage and a decrease of $7.31\,\Omega/\square$ after the first temperature step, but did not reach the starting value. Further temperature steps kept the sheet resistance at similar values. Storing and remeasuring the wafer after this resulted in the expected sheet resistance increase. The additional processes in forming gas atmosphere showed a correction towards the value that was reached at the same temperature in N2 atmosphere. The rest of the processes showed the qualitative behaviour of the boron implanted wafer under these conditions, but even the $1050\,°C$ step was not sufficient to reach the starting value for the phosphorus implanted wafer. These results indicate, that for boron the possible hydrogen passivation was completely negated, while for phosphorus another passivating mechanism might be involved in addition to the hydrogen passivation. They also indicate, that the impact of the temperature is higher than that of the atmosphere during the temperature step.
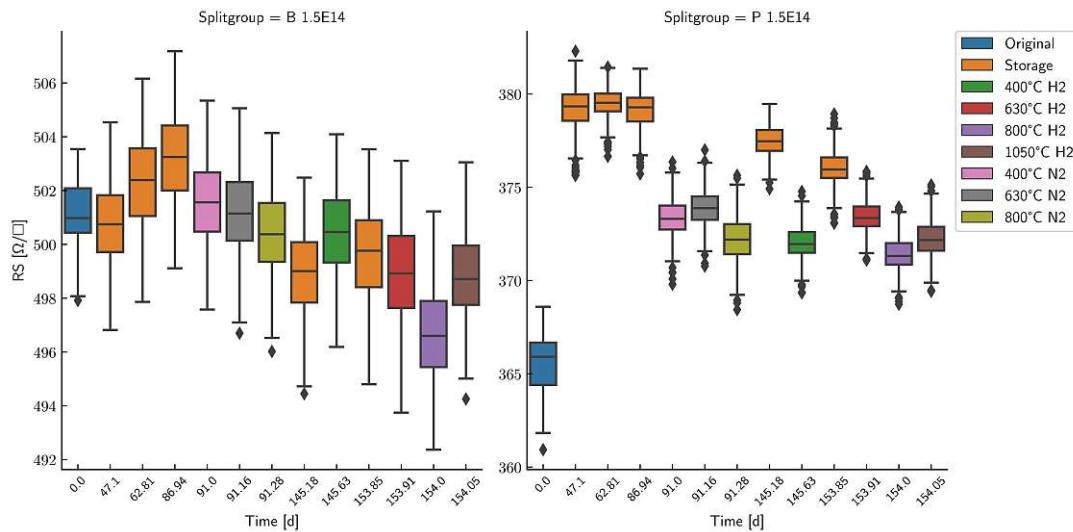
Figure 6.3: Sheet resistance measurement results for boron and phosphorus implanted wafers after storage and temperature steps under N2 or forming gas atmosphere.

6.3 LEIS Measurements

LEIS measurements were performed for 3 wafers with 2 samples per wafer with the conditions outlined in section 3.7. Samples were taken from the wafer edge and wafer middle. Figure 6.4 shows the LEIS spectra at the surface and the depth profiles of the first 4.5 nm

for a wafer implanted with $1.5 \times 10^{14}\,\mathrm{cm}^{-2}$ phosphorus at $115\,\mathrm{keV}$ and $1.5 \times 10^{13}\,\mathrm{cm}^{-2}$ boron at $150\,\mathrm{keV}$ as a counter implant. The wafer was processed according to the general process flow for unstructured wafers. The LEIS measurements were performed 10 months after the implant, anneal and initial measurement. During that time the median sheet resistance of the wafer increased from $376.861\,\Omega/\square$ to $382.494\,\Omega/\square$. The uniformity of the wafer showed no significant change.

Figure 6.4a shows distinctive peaks around $1120\,\mathrm{eV}$, $1710\,\mathrm{eV}$ and $2020\,\mathrm{eV}$. They were attributed to Oxygen, Silicon and Potassium. Silicon and Oxygen were expected for silicon wafers with a native oxide on top. A comparison with fig. 6.4c shows peaks at the same energies, but there seems to be less Potassium in the wafer middle than on the edge.

The depth profiles in fig. 6.4b and fig. 6.4d show that the Potassium depth distribution extends over the whole thickness of the native oxide. At the wafer edge it reaches a thickness of $1.5\,\mathrm{nm}$. In the wafer middle it is slightly thinner with $1.1\,\mathrm{nm}$. The scale for the depth extends from the wafer surface into the direction of the wafer bulk.
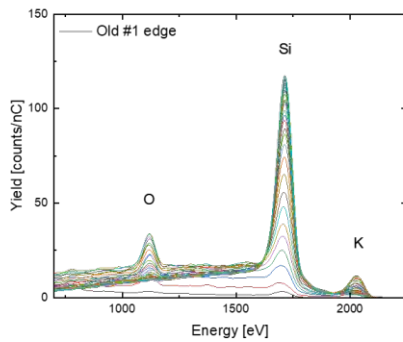
(a) LEIS spectra of wafer edge
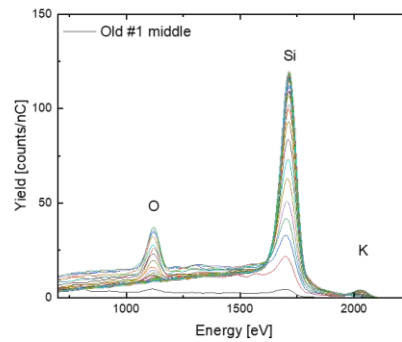
(b) LEIS spectra of wafer middle
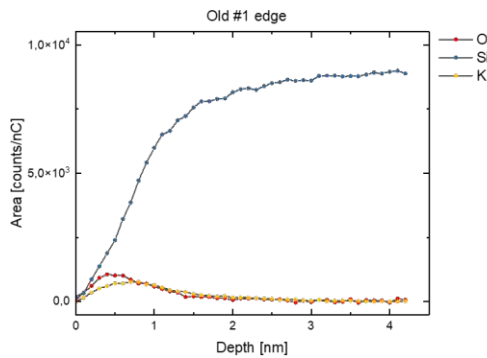
(c) Depth profile of wafer edge
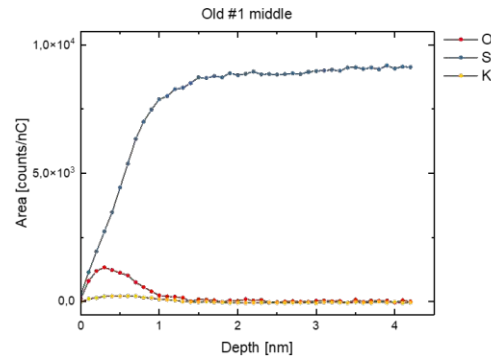
(d) Depth profile of wafer middle

Figure 6.4: LEIS spectra and depth profiles of wafer implanted with $1.5 \times 10^{14}\,\mathrm{cm}^{-2}$ phosphorus measured 10 months after the ion implantation and annealing at the wafer edge and in the wafer middle

Figure 6.5 shows the LEIS spectra at the surface and the depth profiles of the first $4.5\,\mathrm{nm}$ for a wafer implanted with $1.5 \times 10^{14}\,\mathrm{cm}^{-2}$ boron at $45\,\mathrm{keV}$. It was processed alongside the Old 1 wafer with the only difference being the implant species and energy.

During the 10 months between the initial measurement and the last measurement before

the LEIS measurements the sheet resistance increased from $500.475\,\Omega/\square$ to $510.832\,\Omega/\square$. The uniformity over the wafer stayed the same.

The peaks in fig. 6.5a and fig. 6.5c are also located around $1120\,\mathrm{eV}$, $1710\,\mathrm{eV}$ and $2020\,\mathrm{eV}$. There is again more potassium at the edge than in the middle. However, the Potassium peaks are significantly smaller for the boron implanted wafer than for the phosphorus implanted wafer. As seen in fig. 6.5b and fig. 6.5d the native oxide is with $1\,\mathrm{nm}$ in the middle thicker than the $0.8\,\mathrm{nm}$ at the wafer edge. Although only a small amount of Potassium was measured, the depth profiles still indicate, that it is again located in the native oxide. It must be noted, that during the measurement of fig. 6.5d the current of the primary ion gun was higher than for the other measurements, which is responsible for the diminished Silicon signal in this spectrum.
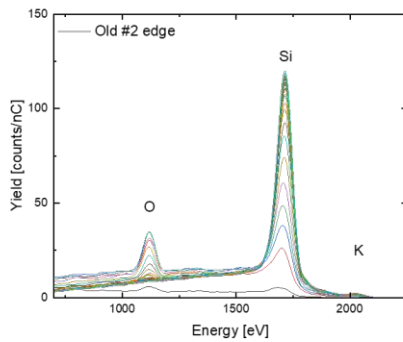
(a) LEIS spectra of wafer edge
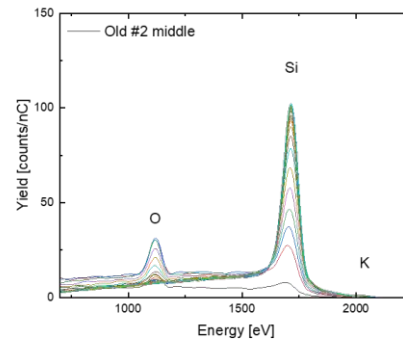
(b) LEIS spectra of wafer middle
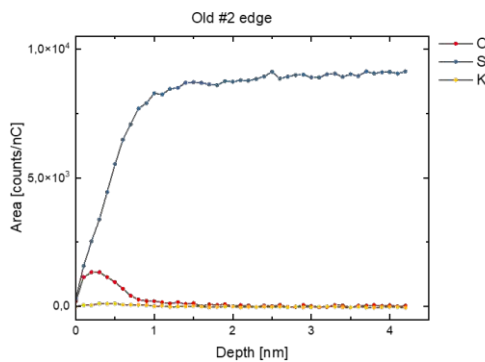
(c) Depth profile of wafer edge
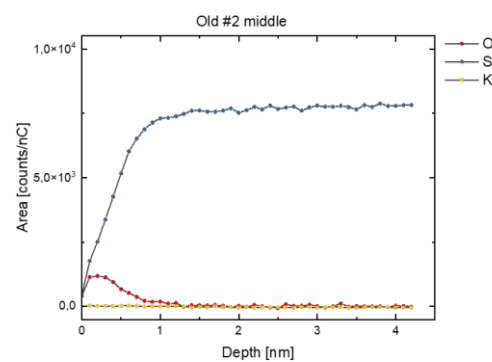
(d) Depth profile of wafer middle

Figure 6.5: LEIS spectra and depth profiles of wafer implanted with $1.5 \times 10^{14}\,\mathrm{cm^{-2}}$ boron measured 10 months after the ion implantation and annealing at the wafer edge and in the wafer middle

To evaluate if the Potassium was accumulated during the months between the ion implantation and the LEIS measurement or if it was already on the wafer in the initial phase, a wafer was processed identical to the boron implanted wafer referred to as Old 2 above and measured with the LEIS as soon as possible. The sheet resistance directly after the implant and annealing processes was $500.859\,\Omega/\square$. The 3 weeks between the implant process and the measurement are due to delays during the shipping process.

As seen in fig. 6.6a and fig. 6.6a there is a slight peak at the energy attributed to Potas-

sium for the sample in the wafer middle, but no Potassium is seen on the wafer edge. The depth profiles are similar to those in fig. 6.5b and fig. 6.5d.
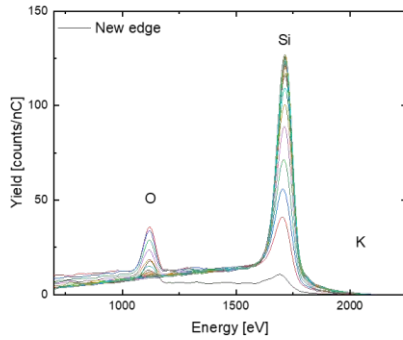
(a) LEIS spectra of wafer edge
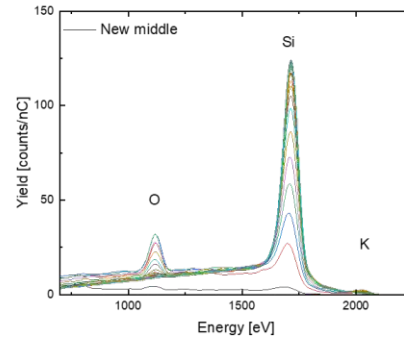
(b) LEIS spectra of wafer middle
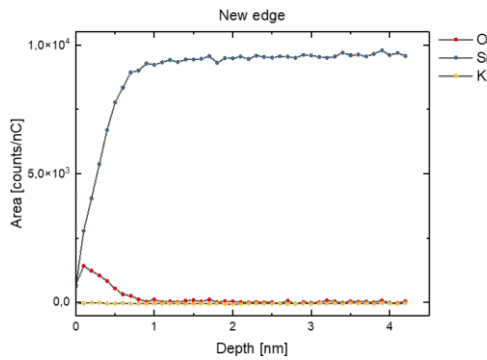
(c) Depth profile of wafer edge
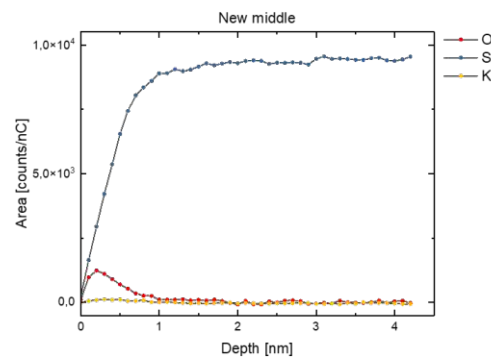
(d) Depth profile of wafer middle

Figure 6.6: LEIS spectra and depth profiles of wafer implanted with $1.5 \times 10^{14}\,\text{cm}^{-2}$ boron measured 3 weeks after the ion implantation and annealing at the wafer edge and in the wafer middle

6.4 VPD Measurements

VPD measurements were performed on wafers implanted under same conditions as those used in section 6.3. Splitgroup B1 was implanted with boron in a dose of $1.5 \times 10^{14}\,\text{cm}^{-2}$ at $45\,\text{keV}$. B2 was implanted with the same dose, split over 5 implant steps. P1 was implanted with $1.5 \times 10^{14}\,\text{cm}^{-2}$ phosphorus at $115\,\text{keV}$ and $1.5 \times 10^{13}\,\text{cm}^{-2}$ boron at $150\,\text{keV}$ as a counter implant. After the implant, anneal and initial sheet resistance measurement, the wafers were stored under clean room conditions for a year before the VPD measurements were performed. Over the course of one year the median sheet resistance for B1 increased by $6.02\,\Omega/\square$, which corresponds to a dose loss of $-1.7\,\%$. B2 showed similar values with a change of $5.35\,\Omega/\square$. For P1 the median sheet resistance increased by $8.78\,\Omega/\square$, which corresponds to a dose loss of $-4.46\,\%$.

The measurement results can be taken from table 6.1. All three splitgroups showed similar boron concentrations, for iron and potassium B1 and P1 were in the same order

Table 6.1: Measured atom concentrations for boron, potassium
and iron given in cm^{-2}

Splitgroup	K	B	Fe
B1	5.3×10^{7}	2.2×10^{12}	1.8×10^{9}
B2	1.2×10^{8}	1.9×10^{12}	2.5×10^{10}
P1	7.4×10^{7}	2.7×10^{12}	5.9×10^{9}

of magnitude, while B2 was one order of magnitude higher.

While Mo, Sr, Zr, Sn, V, W, Pb, Bi, Mg, Ga, Ge, Li, Na, Al, Ca, Cr, Mn, Ni, Co,Sb, Cu, Zn and Ti where measured as well, they showed concentrations very close to the detection limit and were therefore not included in the analysis.

6.5 TXRF Measurements

Three wafers implanted under the same conditions as the ones used for VPD measurements were measured with TXRF a year after the initial sheet resistance measurement following the ion implantation and annealing processes. Figure 6.7 shows the results of the TXRF measurements for one of the boron implanted wafers. As seen in the figure, the only element which was present in concentrations of at least $1 \times 10^{10}\,cm^{-2}$ on the wafer surface was iron. The location of the iron contaminations varied between the three wafers. For the second boron implanted wafer the spot was located at the wafer edge in the bottom right quadrant. For the phosphorous implanted wafer it was also located in the bottom right quadrant, but shifted slightly upwards. On the phosphorous wafer an additional low concentration of Cr was seen in the same location as the Fe. No potassium was observed on any of the wafers.

```
Filename  :TXRF0181.SWP   Group  : B2      Size  : 300 mm    Slot  : 17
X-Ray     :35  kV 255 mA  Points : 277     Time  : 5 sec      Beam  : W-Lb
Date      :23/03/23  01:28:43              Sweep : 300mm
Sample ID :32200702
```
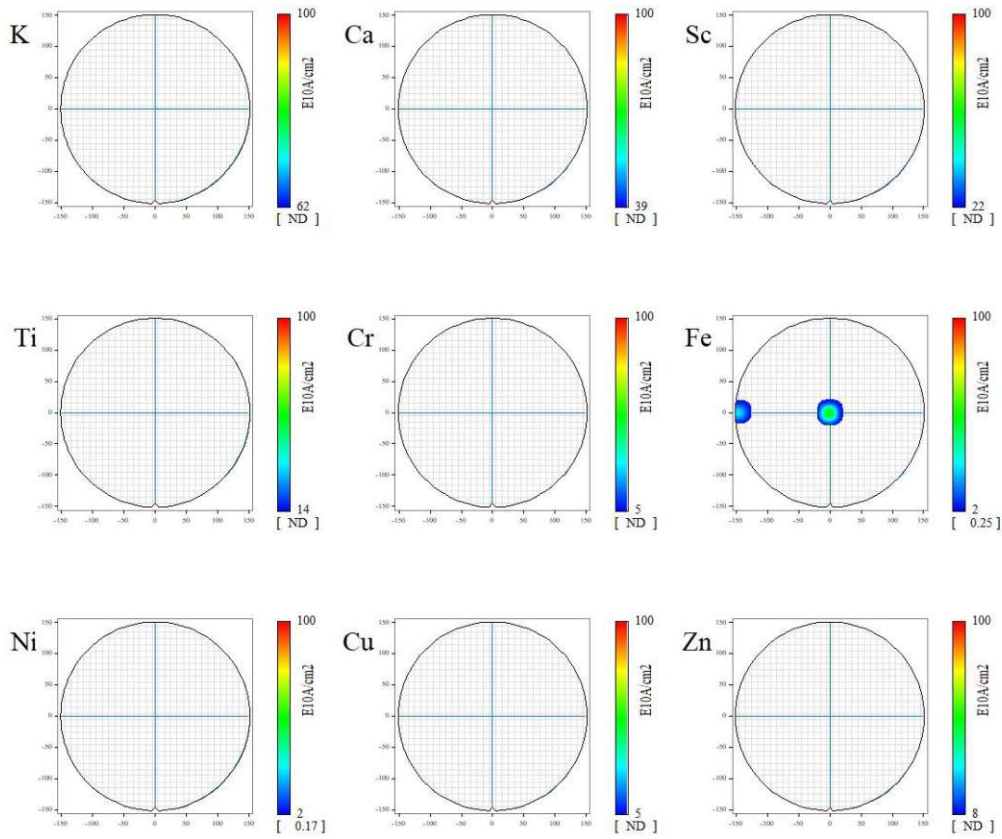

Figure 6.7: Wafermaps of TXRF measurement results of a wafer implanted with Boron

Chapter 7

Discussion

7.1 Unstructured Wafers

7.1.1 Sensitivity and Repeatability

The evaluation of the sensitivity for the individual process steps clearly showed, that the implanted dose has the strongest influence on the measured sheet resistance, closely followed by the energy used for the implant. The energy sensitivity for boron was approximately twice as high as that for phosphorous. This is expected, since 115 keV are necessary to create a dopant depth distribution with phosphorous that is similar to that of boron at 45 keV. A comparison of SRIM simulations for the implant conditions in section 4.1.3 shows that the shift in the boron depth distributions, that is seen in fig. 4.4a for variations of ± 5 keV can be replicated with variations of ± 10 keV for phosphorous.

The scattering oxide showed the third largest influence, while the calculated sensitivities for the substrate dopant concentration and the annealing parameters were judged to be negligible, since they were two orders of magnitude smaller than the values for implant dose and energy. Repeated measurements of implanted wafers showed, that the repeatability for boron is lower than the repeatability for phosphorous implants.

Using eq. (3.11) with the values reported in table 4.1 and the maximum deviations for each process step given in table 3.1, $\sigma_{tot}^2 = 0.477$ for boron and $\sigma_{tot}^2 = 0.958$ for phosphorous. Applying 3.12 results in a gage capability of 6.91 % for boron and 9.79 % for phosphorous. Using the criteria of [29], where a method is suitable for measuring a parameter if GRR%<10 % and maybe acceptable for some uses in the range of 10 % to 30 %, the four-point probe measurement is acceptable for boron implants and barely in the acceptable range for phosphorous.

7.1.2 Multiple Implants

Using multiple smaller implant doses instead of a single implant with a high dose resulted in a significant improvement of the standard variations for sheet resistance measurements on unstructured wafers. It was shown, that for 10 and 15 implant steps the reduction in the standard variation is consistent with the expected reduction by a factor of $\sqrt{n}$, where n is the number of implant steps. This indicates, that the random variations were successfully averaged out. For $n = 5$ a clear reduction was observed, but not to

the expected extend of a factor $\sqrt{5}$, which can be interpreted as partially averaged out random variations. This was observed on wafers implanted on the same tool within two weeks.

The evaluation of the long term stability over a period of 4 months showed a reduction of the Run-to-Run standard deviation for the splitgroup "Multiple Implant without STROX" compared to "Single Implant without STROX" for one of the tested ion implantation tools. For the second ion implanter the effect was reversed, although the difference was smaller. No significant change was observed for the third ion implanter. When the Run-to-Run standard deviation is calculated without regard for the used ion implanter, the Multi Implant shows a deviation, that is 15.48 % lower than the one for the comparable Single Implant group. This could indicate, that the number of implant steps for the Multi Implant group was too low to make the effect observable on all implantation tools.

7.2 Structures

7.2.1 Isolation

The oxide filled trenches worked well as an isolation between individual chips for all tested implant conditions. However, the oxidation process was set up with Oxidation enhanced diffusion, which lead to an expansion of the trench width. This resulted in a slight change of the dimensions of the active area width. The Oxidation enhanced diffusion requires the thick Si3N4 to ensure, that only the trenches are oxidised. Additionally, the nitride layer acts as an isolation between the contact pads and the silicon below them, as well as providing a protection against contamination of the active area. To mitigate the influence of possible nitride thickness variations over the wafer, the 140 nm thick nitride was either completely removed or thinned.

The isolation of the implanted layer to the bulk of the base material was achieved through opposite dopant types of the implanted layer and the base material. As explained in section 2.3 for an abrupt pn-junction the space charge region extends into the area with the lower dopant concentration. The base material could reach a boron concentration of $1.36 \times 10^{15} \, \mathrm{cm}^{-3}$ or a phosphorous concentration of $1.11 \times 10^{14} \, \mathrm{cm}^{-3}$ if the highest possible specification limits were reached. The wafers used for the presented experiments were located in the middle of their respective specification limits. As the concentrations of the implanted layers were above $1 \times 10^{16} \, \mathrm{cm}^{-3}$, the pn-junction was abrupt in every experiment. Since the dopant concentrations were separated by at least two orders of magnitude, variations in the base material should not have a significant influence on the measured resistances. Their influence is most likely in the same order of magnitude as for unstructured wafers.
The epitaxial silicon layer was deposited as undoped as possible within a productive environment. Since the EPI takes on the dopant concentration of the base material, due to diffusion during the high temperature steps, it can be disregarded.

7.2.2 Contact Variations

Of the 4 contact material variations that were evaluated, n-doped poly-Si and TiSi2 with n-doped poly Si could not be used to contact implanted boron layers. This was attributed

to the formation of a pn-junction between the contact material and the implanted layer. If the dopant types differ, as it was the case for experiments with n-doped poly-Si and boron implanted layers, there are two pn-junctions between the sense contacts. Since the directions of the junctions are inverted, the space charge region of one junction is always reduced when a voltage is applied, while the space charge region of the other junction is increased. At least one of the involved junctions is therefore always used in reverse direction and the measurement fails. For the contact variation with n-doped poly-Si, TiSi2 and contact implants, it is likely, that the n-doped poly-Si functioned as an unlimited source for phosphorous diffusion into the region of the contact implant. Using the Arrhenius parameters reported in [44] and a maximum temperature of 1040 °C for the final anneal, the phosphorous concentration 50 nm away from the poly-Si/Si interface is approximately $1 \times 10^{20}\,\mathrm{cm^{-3}}$. The diffused phosphorous would then have compensated the charge carriers of the contact implant and thus eliminated the connection between the implanted layer and the TiSi2 in the trench bottom.

It is therefore evident, that either the contact material and the implanted layer must be of the same dopant type or a diffusion barrier and metal layer must be used between the two.

While Tungsten enabled a good contact to the implanted boron layer, for the chips where the connection remained, it was not a viable option for long-term use, due to the risk of contamination and the bend up of the contact material above the trenches.

The fourth variation which used a Ti/TiN-Liner in combination with n-doped poly-Si was able to contact implanted boron layers. This means, that the ALD liner, which was deposited on the sidewalls and bottom of the contact trench was sufficient as a diffusion barrier for the phosphorous in the poly-Si and prevented the formation of a pn-junction.

If a metal layer is used, the dopant concentration on the semiconductor side of the ms-junction must be high. As explained in section 2.4, this is necessary to ensure an ohmic contact instead of a Schottky contact. For the high implant doses used in the described experiments, this condition is met. An additional contact implant can be used to fulfil this condition if the dose of the active implant is low. This was the case for implants in the low $1 \times 10^{13}\,\mathrm{cm^{-3}}$ range. However, this additional implant must be of the same dopant type as the active implant, have a high dose and it must be shallow. Since this implant process must occur before the contact trenches are filled, the implant is subjected to the following high temperature processes used to anneal the contact material and later to anneal the active implant. The effect of the diffusing contact implant dopants must be taken into account.

7.2.3 Accuracy

All sheet resistances calculated from measured resistances were in good agreement with the calculated values from simulations of the implant conditions. Exceptions occurred, when the implanted dose resulted in charge carrier concentrations below the range of validity for the formulas used to calculate the mobility. Performing the fit on the measured values resulted in fit parameters, which were in good agreement with the fit parameters in table 4.3 for implantations on unstructured wafers, indicating, that the sheet resistances for lower doses in the $1 \times 10^{13}\,\mathrm{cm^{-2}}$ are correct as well. For Boron implants through 60 nm
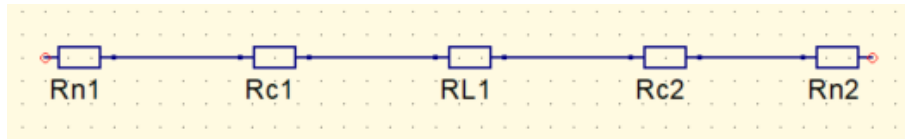
Figure 7.1: Equivalent circuit of chipvariation 6
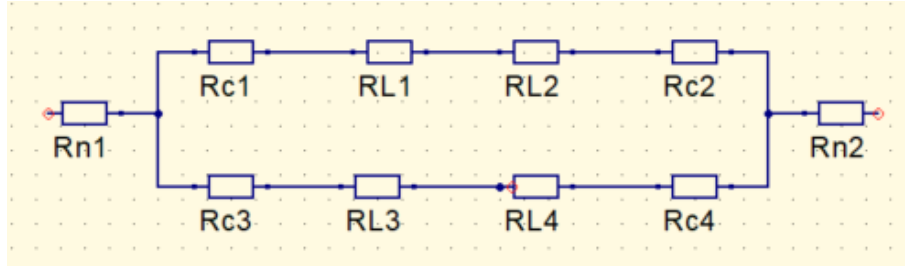
Figure 7.2: Equivalent circuit of chipvariation 7

nitride with ALD Ti/TiN + poly-Si contacts, the fit parameters differed from those on unstructured wafers by $+0.137$ for a and -4.694 for b. For phosphorous implants through $60\,\text{nm}$ nitride with poly-Si contacts, a deviated from the fit on unstructured wafers in the third decimal and b differed by -0.439.

The main concern for accurate measurements were influences that overshadowed the signature of the implanter itself. Such influences were variations in the thickness of the nitride overlying the active area, possible out-diffusion of the contact implant or the dopants from the poly silicon when no diffusion barrier was used and the influence of the measurement itself. The influence of the measurement program was eliminated by norming the measured resistance values on the median of the chipvariations per each measurement site.

For the radial pattern, which was attributed to variations of the nitride thickness over the wafer, a fit was performed on the ΔR [%] values and deducted from the measured resistances. The resulting variations of the resistances over the wafer were within the $\pm 1.5\,\%$ range expected for the implants and showed a stripe-like pattern. However, a twist of the wafers by $90°$ should have resulted in a twist of the stripes. This was not the case. The pattern is therefore not a result of beam current fluctuations over the wafer diameter. Such fluctuations should be seen in the resistance measurements, as they result in local changes of the implanted dose.

The ratios between the measured resistances from chipvariations on a single wafer were generally in good agreement with the expected ratios stated in table 5.1. The exception were the variations 6, 7 and 8. For these chip variations both length and width were doubled, which should have kept the resistance the same. However, in all experiments, where a measurement of the chip variations was possible, the resistance decreased from 6 to 8 with the increase in area. Comparing this effect with the offset that was observed between chipvariations 1 and 4, which had the same length, but different widths, indicates, that the change in width is the deciding factor. Figure 7.1 shows the equivalent circuit for chip variation 6. Rn1 and Rn2 are the resistances between the needles of the measurement tool and the contact material. Rc1 and Rc2 are the resistances of the contact material. RL1 is the resistance of the implanted layer. When both length and width of the active area are doubled, as it is the case for chipvariation 7 in comparison to variation 6, RL1 is expanded with RL2, RL3 and RL4. The serial resistances are due to the doubled length

and the parallel resistances are due to the doubled width. Rn1 and Rn2 stay the same. If the Rc resistances did not change as well, the resistance of both circuits would be the same. However, a wider structure requires additional contact material, resulting in the change in Rc1 and Rc2, which can be described by adding the resistances Rc3 and Rc4. These additional resistances are responsible for the offsets between chipvariations were the width changes.

The presented standard deviations of the implanted dose given in percent generally showed a reduction with increasing length. This was also seen for structures with the same length, but different widths, although the effect was less noticeable for those cases. The high-ohmic structure resulted in most cases in the lowest deviations. It is likely, that the high deviations for chip variation 11 in table 5.3 are due to the fact, that the measured resistances were close to upper limit of the validity range of the measurement program. Therefore it can be concluded, that the chipvariations with bigger active areas offer the highest chance of actually representing the changes in the implanted dose.

7.2.4 Proposed Ideal Process Flow

An ideal process flow should be robust against variations at the individual processes. While the process flow could not be finalized during the course of this thesis, the presented results offer insight into the main difficulties that need to be taken into account.

Isolation

The isolations trenches must be deeper than the concat trenches. The current depth of $4\,\mu m$ should be sufficient for most ion implant energies in productive use. A change to a different oxidation process could mitigate the influence of the isolation trench width on the width of the active area. The nitride is a necessary component to protect the active area, but a thickness of $30\,nm$ should be sufficient to act as a contamination protection and as a scattering layer during the implant. It would be advantageous to start with this nitride thickness. If the filling of the isolation trenches requires a thick nitride layer, it should be removed and replaced by a thin nitride after the oxidation of the trenches. Possible ways to remove the nitride are hot phosphoric acid or a plasma etch process. If hot phosphoric acid is used, the pad oxide below the nitride must be replaced as well, to avoid contaminations with phosphorous.

Contacts

The contact trenches should be shallower than the isolation trenches, but they need to be deep enough to contact the whole implanted layer. Under the assumption of complete nitride and oxide removal over the active area, a trench of $1\,\mu m$ depth would be sufficiently deep to contact a boron implant with up to $250\,keV$ or a phosphorous implant with up to $525\,keV$. For the measurement of implants with higher energies, the depth of the trenches would have to be increased.

Concerning the contact material, it can be concluded, that a poly-Si, that is doped with a high dopant concentration of the same type as the active implant creates a good contact. If a poly-Si of the same contact type is not available, then the alternative contact with an

ALD deposited Ti/TiN liner and a poly-Si filling in combination with a contact implant works as well.

Active Area

Considering the standard deviations for each chipvariation, it would be beneficial to use only variations 3, 7 and 11, as they were the most stable. For a given implant dose, variation 7, 3 and 11 result in low, medium and high resistances respectively. With this it would be possible to use the structures for a wide range of implant doses, since at least one of the structures would be suitable for a measurement.

1	1	1	1	1	1	1	1
2	2	2	2	2	2	2	2
3	3	3	3	3	3	3	3
4	4	4	4	4	4	4	4
5	5	5	5	5	5	5	5
6	6	6	6	6	6	6	6
7	7	7	7	7	7	7	7
8	8	8	8	8	8	8	8
9	9	9	9	9	9	9	9
10	10	10	10	10	10	10	10
11	11	11	11	11	11	11	11

(a) Current Shot Pattern

3	7	11	3	7	11	3	7
11	3	7	11	3	7	11	3
7	11	3	7	11	3	7	11
3	7	11	3	7	11	3	7
11	3	7	11	3	7	11	3
7	11	3	7	11	3	7	11
3	7	11	3	7	11	3	7
11	3	7	11	3	7	11	3
7	11	3	7	11	3	7	11
3	7	11	3	7	11	3	7
11	3	7	11	3	7	11	3

(b) Proposed Shot Pattern

Figure 7.3: Shot pattern currently in use and proposed shot pattern

Figure 7.3a shows the shot pattern used for the test structures in the presented experiments. It includes all chipvariations. A shot pattern, that only includes the variations 3, 7 and 11 is proposed in fig. 7.3b. The variations are no longer arranged in rows with only on variation, but rather mixed. This would allow an easier determination of shot pattern specific influences and every row and column would include structures for all implant doses. To evaluate geometric effects caused by diffusion of dopants from the contact material into the active region or by changes of the isolation trench width, a pattern consisting of variations 2, 4, 5 and 11 could be used. 2 and 4 have the same length, but different widths and from 4 to 5 the width is constant but the length doubles. With this, there are again low and mid ohmic structures present. Within a shot the pattern should be similar to the version in fig. 7.3b, in the sense, that each row should start with a different chipvariation.

7.3 Wafer ageing

The results presented in chapter 6 indicate, that the native oxide and the thin oxide created through the standard clean 2 are not sufficient to protect the wafer from contaminants. The LEIS measurements showed potassium on wafers, that were stored for 10 months, with more potassium at the wafer edges than in the middle. While the VPD measurement did not show a potassium concentration, that would be high enough to account for a change in the sheet resistance, this might be due to the nature of the measurement. For the LEIS measurement two small areas where chosen on the wafer and analysed. During the VPD measurement the droplet that is analysed in the ICP-MS was scanned over the whole wafer. A spatial resolution is therefore not possible and the returned concentration is averaged over the whole wafer.

To achieve spatial resolution TXRF measurements were done. The TXRF showed the presence of iron atoms on the wafer surface on three wafers.

Since the three measurement methods were performed on wafers, that were implanted within a few weeks of each other with the same implant parameters and stored in separate wafer boxes, it is likely that the differences in the measurement results are due to the difference in storage. As the wafers were processed and measured on the same tools before LEIS, VPD and TXRF were performed, the only source of contaminants that are left are the clean room air and the boxes in which the wafers were stored. Joly reported ion implantation, thermal treatment, etching and cleaning as the main sources of metallic contaminations on silicon wafers. [45] Since the wafer boxes were used to store other wafers before the ones used for this thesis, it is possible, that trace amounts of contaminants were left over in the boxes even after a cleaning process. This might account for the difference in the observed contaminant species. Gorodokin and Zemlyanov also mentioned clean-room gloves as a possible source of Fe and K contamination. Handling of equipment parts with clean-room gloves during maintenance could lead to such contaminations, when the equipment comes into contact with the wafer. [46]

As mentioned by Krivec [47], a contamination of sodium ions with a dose of $1 \times 10^{10}\,\mathrm{cm}^{-2}$ at an interface already leads to a change in the threshold voltage of a MOS transistor. Ion concentrations below this value are therefore considered insignificant for this analysis. Chen reported changes in sheet resistance over time for ion implanted silicon wafers. Wafers implanted with n-type dopants showed a fast increase, while for p-type dopants a slow decrease or increase was seen. The changes in sheet resistance were attributed to changes in the surface charges through the growth of an oxide layer and the deposition of contaminants. [26] "Reduction of the fixed surface charge density and increasing of the trap density both force the reduction of N-type layer's carrier density. But the former helps increasing and the latter causes reduction of the carriers in the P-type layer."[26, p.2] The measurement system needle - native oxide - silicon can be approximated as a Metal-Oxide-Semiconductor (MOS) structure. In a real MOS structure interface traps and trapped charges at the SiO2/Si interface, fixed oxide charges, oxide trapped charges and mobile charges can exist and influence the characteristics of the structure. Interface traps can be acceptor or donor like and create charge states within the bandgap. They are dependent on the applied bias. The other charges do not depend on the bias and cause a voltage shift. Sze and Ng likened the fixed oxide charges to "a charge sheet located at the Si-SiO2 interface".[7, p.223] Mobile charges Q_m can, as their name suggests, move

through the oxide in accordance with the applied bias. The corresponding voltage shift is given by eq. (7.1)

$$\Delta V_m = -\frac{Q_m}{C_i} \tag{7.1}$$

C_i denotes the capacitance of the oxide. The voltage shift is added to the flat band voltage. [7]

The effect of the bakeout experiments could be explained as desorption of contaminants during the temperature steps or through diffusion deeper into the material, where their effect on the sheet resistance could be diminished.

Chapter 8

Summary and Outlook

Multiple implants are a suitable way of reducing random variations in ion implantation monitoring. An optimum between the improvement through a higher number of implant steps and process restrictions such as the need for a fast feedback and sufficient accuracy must be found.

The wafer surface is not sufficiently protected after the last HF and SC1 and SC2 clean to account for long storage processes. If a "golden" reference wafer should be used, a defined oxide or nitride layer on top is necessary, as it was already suggested in [7] and [26].

The sheet resistance for boron, phosphorous and arsenic implants with different doses follows the power law of [34].

Metal-semiconductor junctions in combination with contact implants results in good contacts with the implanted layer in the tested structures for both boron and phosphorous implants. The prerequisite for this is the use of a layer, that lines the whole contact trench. Using TiSi2 at the bottom of the trench with a contact implant that envelops the trench is not enough to contact a boron implant if n-doped poly-Si is used to fill the trench. For phosphorous implants it makes no difference, as dopants that diffuse from the poly-Si into the active area supplement the contact implant and do not repress it. A Ti/TiN Liner and a tungsten plugfill process offer a good contact to the implanted layer, but the necessary process steps to produce the structures cause too much stress in the material. The bend up and subsequent breaking of the contact strips poses a significant contamination risk.
The combination of a Ti/TiN liner deposited by ALD and a poly-Si plugfill process is a suitable alternative. The buried liner poses no contamination risk, but the even deposition along the trench walls offers a good contact to the implanted layer in all possible implant depths.

Further experiments are required to test the structures with different implantation energies with the same dose and species. The evaluation of the robustness of the structures concerning variations in the production remains to be done. The combination of the structured wafers with multiple implant steps is of interest as well.

The multiple implant method offers a simple and cost efficient way of improving the accuracy for ion implanter monitoring, without the need for additional equipment. Through the number of implant steps the gain in accuracy can be adjusted as needed. The tested structures on the other hand enable the monitoring of both dopant types in different dose ranges and energies.

Bibliography

[1] G. L. Pearson and J. Bardeen, "Electrical Properties of Pure Silicon and Silicon Alloys Containing Boron and Phosphorus," *Physical Review*, vol. 75, pp. 865–883, Mar. 1949.

[2] F. J. Morin and J. P. Maita, "Electrical Properties of Silicon Containing Arsenic and Boron," *Physical Review*, vol. 96, pp. 28–35, Oct. 1954.

[3] W. Shockley, "FORMING SEMICONDUCTIVE DEVICES BY IONIC BOMBARD-MENT," *United States Patent Office*, vol. US465393A, p. 4, Feb. 1957.

[4] M. A. Wendman and W. Smith, "Thermal wave implant dosimetry for process control on product wafers," *Nuclear Instruments and Methods in Physics Research Section B: Beam Interactions with Materials and Atoms*, vol. 21, pp. 559–562, Jan. 1987.

[5] T. Hara, S. Takahashi, H. Hagiwara, J. Hiyoshi, W. L. Smith, C. Welles, S. K. Hahn, L. Larson, and C. C. D. Wong, "Damage formed by ion implantation in silicon evaluated by displaced atom density and thermal wave signal," *Applied Physics Letters*, vol. 55, pp. 1315–1317, Sept. 1989.

[6] S. Falk, R. Callahan, and P. Lundquist, "Accurate dose matching measurements between different ion implanters," in *Proceedings of 11th International Conference on Ion Implantation Technology*, (Austin, TX, USA), pp. 268–271, IEEE, 1997.

[7] S. M. Sze and K. K. Ng, *Physics of Semiconductor Devices*. Hoboken, N.J: Wiley-Interscience, 3rd ed ed., 2007.

[8] J. Lutz, H. Schlangenotto, U. Scheuermann, and R. De Doncker, *Semiconductor Power Devices*. Cham: Springer International Publishing, 2018.

[9] M. I. Current, L. Rubin, and F. Sinclair, "Commercial Ion Implantation Systems," in *Ion Implantation Science and Technology* (J. F. Ziegler, ed.), Sept. 2018.

[10] F. Sinclair, J. Olson, D. Rodier, A. Eidukonis, T. Thanigaivelan, and S. Todorov, "VIISta 900 3D: Advanced medium current implanter," in *2014 20th International Conference on Ion Implantation Technology (IIT)*, (Portland, OR, USA), pp. 1–4, IEEE, June 2014.

[11] C. R. Harris, K. J. Millman, S. J. van der Walt, R. Gommers, P. Virtanen, D. Cournapeau, E. Wieser, J. Taylor, S. Berg, N. J. Smith, R. Kern, M. Picus, S. Hoyer, M. H. van Kerkwijk, M. Brett, A. Haldane, J. F. del Río, M. Wiebe, P. Peterson, P. Gérard-Marchant, K. Sheppard, T. Reddy, W. Weckesser, H. Abbasi, C. Gohlke,

and T. E. Oliphant, "Array programming with NumPy," *Nature*, vol. 585, pp. 357–362, Sept. 2020.

[12] M. Waskom, "Seaborn: Statistical data visualization," *Journal of Open Source Software*, vol. 6, p. 3021, Apr. 2021.

[13] J. Reback, jbrockmendel, W. McKinney, J. V. den Bossche, T. Augspurger, M. Roeschke, S. Hawkins, P. Cloud, gfyoung, Sinhrks, P. Hoefler, A. Klein, T. Petersen, J. Tratner, C. She, W. Ayd, S. Naveh, JHM. Darbyshire, M. Garcia, R. Shadrach, J. Schendel, A. Hayden, D. Saxton, M. E. Gorelli, F. Li, M. Zeitlin, V. Jancauskas, A. McMaster, T. Wörtwein, and P. Battiston, "Pandas-dev/pandas: Pandas 1.4.2," Apr. 2022.

[14] P. Virtanen, R. Gommers, T. E. Oliphant, M. Haberland, T. Reddy, D. Cournapeau, E. Burovski, P. Peterson, W. Weckesser, J. Bright, S. J. van der Walt, M. Brett, J. Wilson, K. J. Millman, N. Mayorov, A. R. J. Nelson, E. Jones, R. Kern, E. Larson, C. J. Carey, İ. Polat, Y. Feng, E. W. Moore, J. VanderPlas, D. Laxalde, J. Perktold, R. Cimrman, I. Henriksen, E. A. Quintero, C. R. Harris, A. M. Archibald, A. H. Ribeiro, F. Pedregosa, P. van Mulbregt, SciPy 1.0 Contributors, A. Vijaykumar, A. P. Bardelli, A. Rothberg, A. Hilboll, A. Kloeckner, A. Scopatz, A. Lee, A. Rokem, C. N. Woods, C. Fulton, C. Masson, C. Häggström, C. Fitzgerald, D. A. Nicholson, D. R. Hagen, D. V. Pasechnik, E. Olivetti, E. Martin, E. Wieser, F. Silva, F. Lenders, F. Wilhelm, G. Young, G. A. Price, G.-L. Ingold, G. E. Allen, G. R. Lee, H. Audren, I. Probst, J. P. Dietrich, J. Silterra, J. T. Webber, J. Slavič, J. Nothman, J. Buchner, J. Kulick, J. L. Schönberger, J. V. de Miranda Cardoso, J. Reimer, J. Harrington, J. L. C. Rodríguez, J. Nunez-Iglesias, J. Kuczynski, K. Tritz, M. Thoma, M. Newville, M. Kümmerer, M. Bolingbroke, M. Tartre, M. Pak, N. J. Smith, N. Nowaczyk, N. Shebanov, O. Pavlyk, P. A. Brodtkorb, P. Lee, R. T. McGibbon, R. Feldbauer, S. Lewis, S. Tygier, S. Sievert, S. Vigna, S. Peterson, S. More, T. Pudlik, T. Oshima, T. J. Pingel, T. P. Robitaille, T. Spura, T. R. Jones, T. Cera, T. Leslie, T. Zito, T. Krauss, U. Upadhyay, Y. O. Halchenko, and Y. Vázquez-Baeza, "SciPy 1.0: Fundamental algorithms for scientific computing in Python," *Nature Methods*, vol. 17, pp. 261–272, Mar. 2020.

[15] J. D. Hunter, "Matplotlib: A 2D Graphics Environment," *Computing in Science & Engineering*, vol. 9, no. 3, pp. 90–95, 2007.

[16] J. F. Ziegler, M. D. Ziegler, and J. P. Biersack, "SRIM-2013.00."

[17] C. A. Bishop, "Process Diagnostics and Coating Characteristics," in *Vacuum Deposition Onto Webs, Films and Foils*, pp. 85–128, Elsevier, 2015.

[18] B. Spangenberg, G. M. Mladenov, and V. I. Orlinov, "BERECHNUNG DES SCHICHTWlDERSTANDES FOR DIE BOR- IMPLANTATION IN SILIZIUM," *Thin Solid Films*, vol. 71, p. 6, 1980.

[19] M. M. Ghorbani and R. Taherian, "Methods of Measuring Electrical Properties of Material," in *Electrical Conductivity in Polymer-Based Composites: Experiments, Modelling and Applications*, pp. 365–394, Elsevier, 2019.

[20] G. Masetti, M. Severi, and S. Solmi, "Modeling of carrier mobility against carrier concentration in arsenic-, phosphorus-, and boron-doped silicon," *IEEE Transactions on Electron Devices*, vol. 30, pp. 764–769, July 1983.

[21] N. Arora, J. Hauser, and D. Roulston, "Electron and hole mobilities in silicon as a function of concentration and temperature," *IEEE Transactions on Electron Devices*, vol. 29, pp. 292–295, Feb. 1982.

[22] D. Klaassen, "A unified mobility model for device simulation—I. Model equations and concentration dependence," *Solid-State Electronics*, vol. 35, pp. 953–959, July 1992.

[23] S. Reggiani, M. Valdinoci, L. Colalongo, M. Rudan, G. Baccarani, A. Stricker, F. Illien, N. Felber, W. Fichtner, and L. Zullino, "Electron and hole mobility in silicon at large operating temperatures. I. Bulk mobility," *IEEE Transactions on Electron Devices*, vol. 49, pp. 490–499, Mar. 2002.

[24] S. Sze and J. Irvin, "MOBILITY AND IMPURITY LEVELS IN GaAs, Ge, AND Si AT 300°K," *Solid-State Electronics*, vol. 11, pp. 599–602, 1968.

[25] G. Kaiblinger-Grujin, H. Kosina, and S. Selberherr, "Influence of the doping element on the electron mobility in n-silicon," *Journal of Applied Physics*, vol. 83, pp. 3096–3101, Mar. 1998.

[26] J. T. Chen, "Monitoring low dose single implanted layers with four-point probe technology," *Nuclear Instruments and Methods in Physics Research Section B: Beam Interactions with Materials and Atoms*, vol. 21, pp. 526–528, Jan. 1987.

[27] J. F. Ziegler, *Ion Implantation: Science and Technology.* Boston: Academic Press, 2nd ed ed., 1988.

[28] D. M. Hamby, "A review of techniques for parameter sensitivity analysis of environmental models," *Environmental Monitoring and Assessment*, vol. 32, pp. 135–154, Sept. 1994.

[29] M. Down, F. Czubak, G. Gruska, S. Stahley, and D. Benham, *Measurement Systems Analysis.* fourth ed., June 2010.

[30] G. Smets, E. Rosseel, G. Sterckx, J. Bogdanowicz, W. Vandervorst, D. Shaughnessy, J. Matsuo, M. Kase, T. Aoki, and T. Seki, "Transfer From Rs-based To PMOR-based Ion Implantation Process Monitoring," in *ION IMPLANTATION TECHNOLOGY 2101: 18th International Conference on Ion Implantation Technology IIT 2010*, (Kyoto, (Japan)), pp. 426–431, 2011.

[31] P. Brüner, T. Grehl, and H. H. Brongersma, "Low-energy ion scattering (LEIS)," in *Characterization of Nanoparticles*, pp. 419–439, Elsevier, 2020.

[32] D. K. Schroder, *SEMICONDUCTOR MATERIAL AND DEVICE CHARACTERIZATION.* Hoboken, NJ, USA: John Wiley & Sons, Inc., third ed., Apr. 2005.

[33] J. Bauch and R. Rosenkranz, *Physikalische Werkstoffdiagnostik: Ein Kompendium wichtiger Analytikmethoden für Ingenieure und Physiker.* Berlin, Heidelberg: Springer Berlin Heidelberg, 2017.

[34] A. P. Stack, "The relationship between sheet resistance and ion implant dosimetry," *Nuclear Instruments and Methods in Physics Research Section B: Beam Interactions with Materials and Atoms*, vol. 74, pp. 257–258, Apr. 1993.

[35] A. McCarthy and W. Lukaszek, "A new set of electrical test structures for simultaneous single-wafer monitoring of ion implant shadowing, channeling, and dose uniformity," in *Proceedings of the 1991 International Conference on Microelectronic Test Structures*, (Kyoto, Japan), pp. 163–168, IEEE, 1991.

[36] G. S. Virdi, K. Lal, C. Rauthan, B. Pathak, W. Khokle, and S. Gupta, "ON THE ROLE OF FLUORINE IN BF_2^+ IMPLANTED SILICON," *Solid-State Electronics*, vol. 35, pp. 535–540, Apr. 1992.

[37] D. Gomes, V. P. Markevich, A. R. Peaker, and J. Coutinho, "Dynamics of hydrogen in silicon at finite temperatures from first-principles," *physica status solidi (b)*, vol. 259, p. 2100670, June 2022.

[38] D. Barakel, A. Ulyashin, I. Périchaud, and S. Martinuzzi, "N–p Junction formation in p-type silicon by hydrogen ion implantation," *Solar Energy Materials and Solar Cells*, vol. 72, pp. 285–290, Apr. 2002.

[39] B. J. Hallam, P. G. Hamer, A. M. Ciesla née Wenham, C. E. Chan, B. Vicari Stefani, and S. Wenham, "Development of advanced hydrogenation processes for silicon solar cells via an improved understanding of the behaviour of hydrogen in silicon," *Progress in Photovoltaics: Research and Applications*, vol. 28, pp. 1217–1238, Dec. 2020.

[40] B. Sopori, X. Deng, J. Benner, A. Rohatgi, P. Sana, S. Estreicher, Y. Park, and M. Roberson, "Hydrogen in silicon: A discussion of diffusion and passivation mechanisms," *Solar Energy Materials and Solar Cells*, vol. 41–42, pp. 159–169, June 1996.

[41] J. A. T. De Guzman, V. P. Markevich, J. Coutinho, N. V. Abrosimov, M. P. Halsall, and A. R. Peaker, "Electronic Properties and Structure of Boron–Hydrogen Complexes in Crystalline Silicon," *Solar RRL*, vol. 6, p. 2100459, May 2022.

[42] J. N. Klug, J. Lutz, and J. B. Meijer, "N-type doping of silicon by proton implantation," in *Proceedings of the 2011 14th European Conference on Power Electronics and Applications*, pp. 1–7, 2011.

[43] D. Barakel, A. Ulyashin, I. Périchaud, and S. Martinuzzi, "N–p Junction formation in p-type silicon by hydrogen ion implantation," *Solar Energy Materials and Solar Cells*, vol. 72, pp. 285–290, Apr. 2002.

[44] J. S. Christensen, H. H. Radamson, A. Yu. Kuznetsov, and B. G. Svensson, "Phosphorus and boron diffusion in silicon under equilibrium conditions," *Applied Physics Letters*, vol. 82, pp. 2254–2256, Apr. 2003.

[45] J.-P. Joly, "Metallic contamination assessment of Silicon wafers," *Microelectronic Engineering*, vol. 40, pp. 285–294, Nov. 1998.

[46] V. Gorodokin and D. Zemlyanov, "Metallic contamination in silicon processing," in *2004 23rd IEEE Convention of Electrical and Electronics Engineers in Israel*, (Tel-Aviv, Israel), pp. 157–160, IEEE, 2004.

[47] S. Krivec, *Investigations of Mobile Ion Transport Processes in Thin Layers upon Bias-Temperature Stress.* PhD thesis, Technische Universität Wien, Vienna, May 2011.

Chapter 9

Copyright

/publications/rights/rights_link.html to learn how to obtain a License from RightsLink.

If applicable, University Microfilms and/or ProQuest Library, or the Archives of Canada may supply single copies of the dissertation.

CCC | Marketplace

This is a License Agreement between Technische Universität Wien ("User") and Copyright Clearance Center, Inc. ("CCC") on behalf of the Rightsholder identified in the order details below. The license consists of the order details, the Marketplace Permissions General Terms and Conditions below, and any Rightsholder Terms and Conditions which are included below.

All payments must be made in full to CCC in accordance with the Marketplace Permissions General Terms and Conditions below.

Order Date	31-Mar-2023	Type of Use	Republish in a thesis/dissertation
Order License ID	1340375-1	Publisher	Wiley-Interscience
ISBN-13	9780471143239	Portion	Excerpt (up to 400 words)

LICENSED CONTENT

Publication Title	Physics of Semiconductor Devices	Country	United States of America
Author/Editor	Sze, S. M., Ng, Kwok Kwok	Rightsholder	John Wiley & Sons - Books
Date	01/01/2007	Publication Type	Book
Language	English		

REQUEST DETAILS

Portion Type	Excerpt (up to 400 words)	Distribution	Worldwide
Number of Excerpts	2	Translation	Original language of publication
Format (select all that apply)	Print, Electronic	Copies for the Disabled?	No
Who Will Republish the Content?	Academic institution	Minor Editing Privileges?	Yes
Duration of Use	Life of current edition	Incidental Promotional Use?	No
Lifetime Unit Quantity	Up to 499	Currency	EUR
Rights Requested	Main product		

NEW WORK DETAILS

Title	Fabrication and Evaluation of Test Structures for Precise Dose Control of Ion Implantation Equipment in Semiconductor Manufacturing	Institution Name	Technische Universität Wien
		Expected Presentation Date	2023-05-01
Instructor Name	Markus Valtiner		

ADDITIONAL DETAILS

The Requesting Person/Organization to Appear on the License	Technische Universität Wien

REQUESTED CONTENT DETAILS

Title, Description or Numeric Reference of the Portion(s)	p. 81, p. 223	Title of the Article/Chapter the Portion Is From	p-n Junctions, Metal-Insulator-Semiconductor Capacitors
Editor of Portion(s)	N/A	Author of Portion(s)	Sze, S. M.; Ng, Kwok Kwok
Volume of Serial or Monograph	3	Publication Date of Portion	2007-01-01
Page or Page Range of Portion	p. 81, p.223		

75

CCC | Marketplace

Order Date	31-Mar-2023	Type of Use	Republish in a thesis/dissertation
Order License ID	1340391-1	Publisher	Elsevier
ISBN-13	9780323296441	Portion	Excerpt (up to 400 words)

LICENSED CONTENT

Publication Title	Vacuum Deposition onto Webs, Films and Foils	Country	United States of America
		Rightsholder	Elsevier Science & Technology Journals
Author/Editor	Bishop, Charles	Publication Type	Book
Date	08/18/2015		
Language	English		

REQUEST DETAILS

Portion Type	Excerpt (up to 400 words)	Distribution	Worldwide
Number of Excerpts	1	Translation	Original language of publication
Format (select all that apply)	Print, Electronic	Copies for the Disabled?	No
Who Will Republish the Content?	Academic institution	Minor Editing Privileges?	Yes
Duration of Use	Life of current edition	Incidental Promotional Use?	No
Lifetime Unit Quantity	Up to 499	Currency	EUR
Rights Requested	Main product		

NEW WORK DETAILS

Title	Fabrication and Evaluation of Test Structures for Precise Dose Control of Ion Implantation Equipment in Semiconductor Manufacturing	Institution Name	Technische Universität Wien
		Expected Presentation Date	2023-05-01
Instructor Name	Markus Valtiner		

ADDITIONAL DETAILS

Order Reference Number	N/A	The Requesting Person/Organization to Appear on the License	Technische Universität Wien

REQUESTED CONTENT DETAILS

Title, Description or Numeric Reference of the Portion(s)	part of a sentence on p. 89	Title of the Article/Chapter the Portion Is From	Process Diagnostics and Coating Characteristics
Editor of Portion(s)	N/A	Author of Portion(s)	Bishop, Charles
Volume of Serial or Monograph	N/A	Issue, if Republishing an Article From a Serial	N/A
Page or Page Range of Portion	89	Publication Date of Portion	2015-08-18

RIGHTSHOLDER TERMS AND CONDITIONS

CCC | Marketplace

Order Date	02-Apr-2023	Type of Use	Republish in a thesis/dissertation
Order License ID	1340740-1	Publisher	ELSEVIER BV
ISSN	0168-583X	Portion	Excerpt (up to 400 words)

LICENSED CONTENT

Publication Title	Nuclear instruments & methods in physics research. Section B, Beam interactions with materials and atoms	Publication Type	Journal
		Start Page	526
Article Title	Monitoring low dose single implanted layers with four-point probe technology	End Page	528
		Issue	1
Date	01/01/1984	Volume	21
Language	Dutch		
Country	Netherlands		
Rightsholder	Elsevier Science & Technology Journals		

REQUEST DETAILS

Portion Type	Excerpt (up to 400 words)	Distribution	Worldwide
Number of Excerpts	2	Translation	Original language of publication
Format (select all that apply)	Print, Electronic	Copies for the Disabled?	No
Who Will Republish the Content?	Academic institution	Minor Editing Privileges?	Yes
Duration of Use	Life of current edition	Incidental Promotional Use?	No
Lifetime Unit Quantity	Up to 499	Currency	EUR
Rights Requested	Main product		

NEW WORK DETAILS

Title	Fabrication and Evaluation of Test Structures for Precise Dose Control of Ion Implantation Equipment in Semiconductor Manufacturing	Institution Name	Technische Universität Wien
		Expected Presentation Date	2023-05-01
Instructor Name	Markus Valtiner		

ADDITIONAL DETAILS

Order Reference Number	N/A	The Requesting Person/Organization to Appear on the License	Technische Universität Wien

REQUESTED CONTENT DETAILS

Title, Description or Numeric Reference of the Portion(s)	formula and description on p. 1, 2 sentences on p.2	Title of the Article/Chapter the Portion Is From	Monitoring low dose single implanted layers with four-point probe technology
Editor of Portion(s)	Chen, James T.C.	Author of Portion(s)	Chen, James T.C.
Volume of Serial or Monograph	21	Issue, if Republishing an Article From a Serial	1
Page or Page Range of Portion	526-528	Publication Date of Portion	1987-01-01